Comparing multivariable uncertain model structures for data-driven robust control
Visualization and application to a continuously variable transmission

Tacx, Paul; Oomen, Tom

Important note
To cite this publication, please use the final published version (if applicable).
Please check the document version above.

WILEY

Comparing multivariable uncertain model structures for data-driven robust control: Visualization and application to a continuously variable transmission

Paul Tacx[1] | **Tom Oomen[1,2]**

[1]Control Systems Technology, Department of Mechanical Engineering, Eindhoven University of Technology, Eindhoven, The Netherlands

[2]Delft Center for Systems and Control, Faculty of Mechanical, Maritime, and Materials Engineering, Delft University of Technology, Delft, The Netherlands

Correspondence
Paul Tacx, Control Systems Technology, Department of Mechanical Engineering, University of Technology Eindhoven, Eindhoven, The Netherlands.
Email: p.j.m.m.tacx@tue.nl

Abstract

The selection of uncertainty structures is an important aspect of system identification for robust control. The aim of this paper is to provide insight into uncertain multivariable systems for robust control. A unified method for visualizing model sets is developed by generating Bode plots of multivariable uncertain systems, both in magnitude and phase. In addition, these model sets are compared from the viewpoint of the control objective, allowing a quantitative analysis as well. An experimental case study on an automotive transmission application demonstrates these connections and confirms the importance of the developed framework for control applications. In addition, the experimental results provide new insights into the shape of associated model sets by using the presented visualization procedure. Both the theoretical and experimental results confirm that a recently developed robust-control-relevant uncertainty structure outperforms general dual-Youla-Kučera uncertainty, which in turn outperforms traditional uncertainty structures, including additive uncertainty.

KEYWORDS
Bode plot, control applications, identification for control, multivariable control systems, robust control, uncertain systems

1 | INTRODUCTION

Model errors are a principal aspect of the modeling of physical systems. For instance, in the mechatronic industry, models are becoming increasingly important for control. In particular, stringent demands regarding speed and accuracy leads to the situation where multivariable controllers are required.[1] Model-based controllers effectively deal with inherently multivariable systems.[2] However, discrepancies between the model and the true system may lead to a dramatic deterioration of performance and even instability when implementing a model-based controller on the true system.[3] This paper focuses on robust control which explicitly deals with systematic model errors by designing a controller that stabilizes and achieves a certain guaranteed performance for a model set.[4]

The availability of reliable and systematic robust control algorithms has spurred the development of identification approaches of multivariable model sets for robust control. It has led to approaches that consider parametric uncertainty that is directly applicable to $\mathcal{H}_\infty$ optimization.[5] In References 6 and 7, connections to the prediction error framework

have been established. Besides the use of parameter uncertainty, uncertainty structures in robust control have been further developed towards system identification. First, (inverse) additive and multiplicative uncertainty structures have been developed, for example, Reference 8. These uncertainty structures have been extended towards (normalized) coprime factor perturbations, see References 9 and 10, to deal with closed-loop operation and to accommodate the control goal. These coprime factor-based uncertainty structures have been further refined towards dual-Youla-Kučera uncertainty structures, see References 11-14, that improve the connection between identification and control by explicitly considering the closed-loop operation of the system. Recently, in References 15 and 16, these coprime factor-based uncertainty structures are further refined to explicitly connect the size of uncertainty and the control criterion. An essential advantage of the latter structure is that it provides an inherent scaling of the uncertainty channels that is essential for the nonconservative identification of model sets.

Over the last decades, many uncertainty structures for robust control have been developed, however, generic guidelines, analysis, and comparison of the practical implications of the selection of uncertainty structures have not been thoroughly developed. In Reference 17, several uncertainty structures are experimentally compared on an automotive application. However, no explicit connection is established with identification and the results are not theoretically supported. In Reference 14, it is observed that if the nominal model and the weighting filters are allowed to vary, then many of these uncertainty structures can be explicitly related in terms of circular bounds in the frequency domain. However, such a frequency domain analysis does not explicitly address stability aspects, which is essential if $\mathcal{H}_\infty$-norm-bounded uncertainty is used. In addition, this paper aims to address uncertainty structures for a fixed nominal model, as this is a common scenario in identification for robust control approaches, including[15,18,19]

Although uncertainty structures for robust control are significantly developed and their theoretical advantages on an abstract level have been well established, generic methods to analyze their advantages, consequences, and detailed insights for practical robust control applications are still limited. In particular, the trend toward more advanced uncertainty structures and the multivariable aspects complicate comparison and hampers insight into the underlying structure in view of robust control. The aim of this paper is to develop a generic visualization method for providing practical insight into the performance and robustness characteristics of uncertain multivariable systems for robust control in the setting presented in for example, Reference 20.

The main aim of this paper is visualization which is a principal part of extracting insight, comparison, robustness and performance analysis of control systems. A key example is the Bode plot.[21,22] The Bode plot of SISO systems is based on the polar description of the complex number. Consequently, the Bode plot contains the magnitude and phase. In addition, the polar decomposition naturally connects the Bode plot with the Nyquist plot which is widely used for stability, and robustness analysis.[20] The close relationship between magnitude and phase is underlined by the Bode gain-phase relation and robustness criteria such as gain and phase margin.[20] Frequency response function-based approaches are also used in for example, for nonlinear systems[23] and LPTV systems.[24]

The Bode plot of SISO systems has been extended in several directions to multivariable systems without uncertainty. Often an element-wise Bode plot is considered based on the elements of the frequency response function. However, the element-wise Bode plot becomes unclear as the number of plots inflates if the number of inputs and outputs increases. In Reference 22, the principal magnitude and phase, that is, a multivariable magnitude and phase, are introduced based on the multivariable polar decomposition in Reference 25. The principal magnitude coincides with the wide-accepted multivariable magnitude definition based on the singular values.[20] The combination of the principal magnitude and phase allows for the generation of a generalized Nyquist plot and the analysis of robustness by gain and phase margins.[22]

Despite its relevance, a generic method multivariable Bode analysis method for uncertain multivariable systems is not available in its full generality. In the SISO case, uncertainty structures reduce to a Möbius transformation that allows computing the magnitude and phase analytically.[26] However, extending the Möbius transformation to multivariable systems is not straightforward. In Reference 26, generalizations of the multivariable magnitude are made based on the generalized and skewed structured singular values.[4] However, a (multivariable) phase counterpart is lacking. The principal phase is a suitable measure of the multivariable phase, yet extending the principal phase to uncertain systems is not straightforward. Alternatively, uncertain systems are analyzed in the quadratic constraint framework.[27] The quadratic constraint framework is used to analyze uncertain systems for robust control, for example, in Reference 28 to analyze multivariable phase margins, in Reference 29 to study robustness, and in Reference 30 to study robustness with phase information. The key obstruction of the principal phase for uncertain systems is that the underlying eigenvalue problem is not necessarily convex. Eigenvalues can be approximated by the numerical range, which is convex.[25] The numerical range is used for stability analysis with phase information of uncertain systems in References 28-30.

The main contribution of this paper is the development of a unified method for constructing multivariable Bode plots in magnitude and phase sense of uncertain multivariable systems with the following subcontributions.

(C1) A generic method for multivariable uncertain Bode plots.
    (C1.1) Element-wise Bode magnitude and phase.
    (C1.2) Multivariable Bode magnitude and phase.
(C2) Experimental case study.
    (C2.1) CVT application.
    (C2.2) Overview of uncertainty structures for robust control.
    (C2.3) Overview of considerations.

The novelty in this paper lies in the derivation and application of a generic method for Bode plots of multivariable uncertain systems to enhance insight in uncertain systems for robust control which, while making use of the previous result,[31] has not been published in its full generality. The results in References [28-31] can be retrieved as a special case. This paper extends to the previous results in Reference [26] by proposing a generic method for Bode plots, in both magnitude and phase sense, of uncertain multivariable systems. Although the results in this paper can be generalized to nonsquare systems, in this paper square systems are considered throughout since the aim is to provide practical insight regarding both performance and robustness. For analyzing robustness, the loop gain should be considered which is square by definition. To facilitate the exposition, most of the results are stated in the continuous time domain. However, all results are directly applicable to the discrete-time systems as well, especially since most computations here involve complex matrices and can be applied to discrete-time frequency response functions directly.

Notation. A matrix $A \in \mathbb{H}$ is a Hermitian matrix, that is, a square complex matrix that is equal to the conjugate transpose ($A = A^*$). The eigenvalues of a matrix square matrix $G \in \mathbb{C}^{n \times n}$ are denoted by $\lambda(G)$. The singular values of a (non)square matrix $B \in \mathbb{C}^{n \times m}$ are denoted by $\sigma(B)$. The largest and smallest singular values are denoted by $\overline{\sigma}(B)$ and $\underline{\sigma}(B)$. The function space $\mathcal{H}_\infty^{n \times m}$ are all complex-valued matrix functions which are analytic in the open right-half complex plane $\mathbb{C}^+$ and have a finite $\mathcal{H}_\infty$-norm (i.e., $\|G\|_\infty \sup_{\lambda > 0, \omega \in \mathbb{R}} \overline{\sigma}(G(\lambda + i\omega)) < \infty$). The function space $\mathcal{RH}_\infty^{n \times m} \subset \mathcal{H}_\infty^{n \times m}$ is the subspace of all real-rational and proper transfer matrices without poles in the closed right-half plane. The pair $\{N, D\}$ is an RCF of P if i) $P = ND^{-1}$, ii) $N, D \in \mathcal{RH}_\infty$, and iii) $\exists X, Y \in \mathcal{RH}_\infty$ such that $XN + YD = I$. The pair $\{\tilde{N}, \tilde{D}\}$ is an LCF of P if $\{\tilde{N}^*, \tilde{D}^*\}$ is an RCF of P^*. The LCF is a normalized LCF if, in addition, $DD^* + NN^* = I$. The pair $\{\tilde{N}, \tilde{D}\}$ is an LCF with co-inner numerator of P if it is an LCF of P and, in addition, $\tilde{N}\tilde{N}^* = I$. The matrix blockdiag$(A_1, A_2, \dots)$ denotes a block diagonal matrix whose diagonal blocks are $A_1, A_2, \dots$. The upper linear fractional transformation (LFT) is given by $\mathcal{F}_u(\hat{H}, \Delta) = \hat{H}_{22} + \hat{H}_{21}\Delta(I - \hat{H}_{11}\Delta)^{-1}\hat{H}_{12}$.

2 | PROBLEM FORMULATION AND OUTLINE

2.1 | Robust control setup

The robust control approach in Reference [20](section 8.6) is adopted which is specified by the $\mathcal{H}_\infty$-norm-based criterion

$$\mathcal{J}(P, C) := \|WT(P, C)V\|_\infty, \tag{1}$$

where $W = \text{blockdiag}(W_y, W_u)$, $V = \text{blockdiag}(V_2, V_1)$, and $W, V, W^{-1}, V^{-1} \in \mathcal{RH}_\infty$ are user-defined weighting filters. The closed-loop feedback interconnection $T(P, C)$, see Figure 1, is defined as

$$T(P, C) : \begin{bmatrix} r_2 \\ r_1 \end{bmatrix} \mapsto \begin{bmatrix} y \\ u \end{bmatrix} = \begin{bmatrix} P \\ I \end{bmatrix}(I + CP)^{-1}\begin{bmatrix} C & I \end{bmatrix}. \tag{2}$$

Herein, u denotes the plant input, y denotes the output, r_2 denotes the reference signal, and r_1 denotes the feedforward signal. The criterion (1) in conjunction with the four-block interconnection encompasses many relevant $\mathcal{H}_\infty$-design problems, including the loop-shaping approach in Reference [32], and facilitates the synthesis of internally stabilizing controllers. The criterion (1) is formulated such that it is to be minimized for the true system P_o, that is,
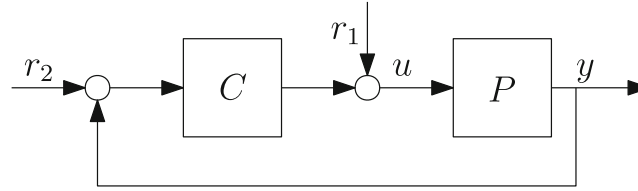
FIGURE 1   Closed-loop feedback interconnection.

$C^{\mathrm{o}} = \arg\min_C \mathcal{J}(P_o, C)$. In general, a full description of the true system P_o is not available. Consequently, C^{o} cannot be determined explicitly.

Alternatively, the controller C^{o} can be approximated by a parametric nominal model $\hat{P}$ of the true system P_o, that is, $\hat{C} = \arg\min_C \mathcal{J}(\hat{P}, C)$. However, discrepancies between the nominal model and the true system may lead to robustness and stability issues.

The key idea in robust control is to consider a model set $\mathcal{P}$ that encompasses the true system P_o, that is, it satisfies

$$P_o \in \mathcal{P}. \tag{3}$$

Associated with the model set is the worst-case performance criterion

$$\mathcal{J}_{\mathrm{WC}}(\mathcal{P}, C) := \sup_{P \in \mathcal{P}} \mathcal{J}(P, C).$$

Consequently, by minimizing the worst-case performance criterion

$$C^{\mathrm{RP}} = \arg\min_C \mathcal{J}_{\mathrm{WC}}(\mathcal{P}, C) \tag{4}$$

it is guaranteed that

$$\mathcal{J}(P_o, C^{\mathrm{RP}}) \leq \mathcal{J}_{\mathrm{WC}}(\mathcal{P}, C^{\mathrm{RP}}). \tag{5}$$

The key point is that robust performance, see for example Reference 20(section 8.6), is guaranteed by (5). The model set is constructed by considering a perturbation Δ around a nominal model $\hat{P}$

$$\mathcal{P} = \left\{ P \middle| P = \mathcal{F}_u(\hat{H}, \Delta), \Delta \in \mathbf{\Delta} \right\}. \tag{6}$$

The transfer matrix $\hat{H}$, see Figure 2, is based on the upper linear fractional transformation

$$\hat{H} : \begin{bmatrix} p \\ u \end{bmatrix} \mapsto \begin{bmatrix} q \\ y \end{bmatrix} = \begin{bmatrix} \hat{H}_{11} & \hat{H}_{12} \\ \hat{H}_{21} & \hat{H}_{22} \end{bmatrix}, \tag{7}$$

where p and q denote the exogenous input and output respectively. The transfer matrix $\hat{H}$ contains the (multivariable) nominal model $\hat{P}$ and determines the internal structure of the model set. The perturbation set is a norm-bounded subset of $\mathcal{H}_\infty$

$$\mathbf{\Delta} = \left\{ \Delta \in \mathcal{RH}_\infty \middle| \|\Delta\|_\infty \leq \gamma, \mathrm{blockdiag}(\Delta_1, \ldots, \Delta_{n_u}) \right\}. \tag{8}$$

The parameter γ defines the $\mathcal{H}_\infty$-norm bound. The uncertainty set can be subject to additional constraints, such as parameter uncertainty from a polytope.[27,33] Note that (8) encompasses unstructured uncertainty

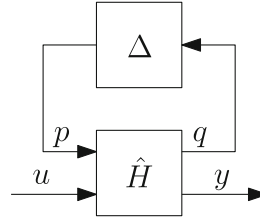$$\mathbf{\Delta_u} = \left\{ \Delta_u \in \mathcal{RH}_\infty \middle| \|\Delta_u\|_\infty \leq \gamma \right\}. \tag{9}$$

FIGURE 2 Upper LFT plant setup.

TABLE 1 Comparison of uncertain model sets.

	Candidate open-loop models P in (6)	Worst-case closed-loop performance
$\mathcal{P}^{\text{Add}}$, see (15)	$\hat{P} + \Delta_u$	$\mathcal{J}_{\text{WC}}(\mathcal{P}^{\text{Add}}, C^{\text{exp}}) \leq \sup_{\Delta_u \in \Delta_u} \|\hat{M}_{22} + \hat{M}_{21}\Delta_u(I - \hat{M}_{11}\Delta_u)^{-1}\hat{M}_{12}\|_\infty$
$\mathcal{P}^{\text{dY}}$, see (18)	$(\hat{N} + D_c\Delta_u)(\hat{D} - N_c\Delta_u)^{-1}$	$\mathcal{J}_{\text{WC}}(\mathcal{P}^{\text{dY}}, C^{\text{exp}}) = \sup_{\Delta_u \in \Delta_u} \|\hat{M}_{22} + \hat{M}_{21}\Delta_u\hat{M}_{12}\|_\infty$

Throughout, unless otherwise stated, unstructured uncertainty perturbations are considered to improve the readability of the results.

2.2 | Motivating example

The main motivation for this paper stems from the observation that the resulting performance guarantee in (5) hinges on the shape and size of the model set $\mathcal{P}$. In particular, the choice of uncertainty structure influences the worst-case performance criterion (5). The control criterion (5) is related to the interconnection of the model set and the controller

$$\mathcal{J}_{\text{WC}}(\mathcal{P}, C) = \sup_{\Delta_u \in \Delta_u} \left\| \mathcal{F}_u\left(\hat{M}, \Delta_u\right) \right\|_\infty.$$

Here, the matrix $\hat{M}$ depends on the internal structure of the uncertainty structure determined by (7) and the controller C.

Commonly, additive and multiplicative uncertainty structures are considered. However, also more refined uncertainty structures are considered based on the dual-Youla-Kučera structure, see Table 1. The dual-Youla-Kučera-based model sets possess specific advantageous properties when compared to traditional uncertainty structures that are outlined in Section 3. Roughly speaking, these structures lead to an affine expression in Δ_u on *closed-loop* performance. However, since $\hat{H}_{11}^{\text{dY}} \neq 0$, the *open-loop* model characteristics in (6) involve the general form of an LFT and do not reduce to an affine expression as with, for example, additive uncertainty structures. A key consequence of Table 1 is that it is not straightforward to interpret the certain and uncertain *open-loop* model aspects associated with the model set $\mathcal{P}^{\text{dY}}$. This is confirmed by the following example.

Example 1. Consider a model $\hat{P} = 3$ and controller C with coprime factor frequency response function evaluated at a single frequency ω given by $\hat{N} = 2$, $\hat{D} = 1$, $N_c = -\frac{5}{2}$, $D_c = \frac{9}{4}$. To illustrate the results with respect to the minimum and maximum gain, the norm-bound and the perturbation model is varied, that is, $\Delta_u \in \mathbb{C}$, $\overline{\sigma}(\Delta_u) \leq \gamma$, $\gamma = \{0.1, 0.4, 1\}$. Random realizations of admissible perturbations Δ_u are generated that satisfy the norm-bound γ. The corresponding models $P \in \mathcal{P}^{\text{Add}}$ and $P \in \mathcal{P}^{\text{dY}}$, see Table 1, are depicted in Figure 3 and 4 respectively.

Example 1, and in particular Figures 3 and 4, reveal that the dual-Youla-Kučera model sets $\mathcal{P}^{\text{dY}}$ exhibits a significantly different behavior when compared model sets based on additive uncertainty structures, for example, Figure 3. Indeed, for additive structures, the nominal model $\hat{P}$ is the center of the circular model set, independent of the $\mathcal{H}_\infty$-norm bound γ. The size of the model set grows proportional to γ. Interestingly, this specific behavior is not necessarily present for dual-Youla-Kučera-based structures, see Figure 4.

1. For $\gamma = 0.1$: the dual-Youla-Kučera model set is circular yet centered around 2.08, which is not equal to the nominal model response $\hat{P} = 2$.
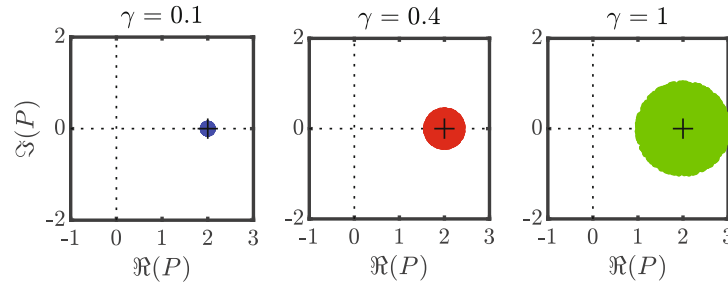
FIGURE 3 Generated candidate additive models $P \in \mathcal{P}^{\text{Add}}$ corresponding to Example 1.
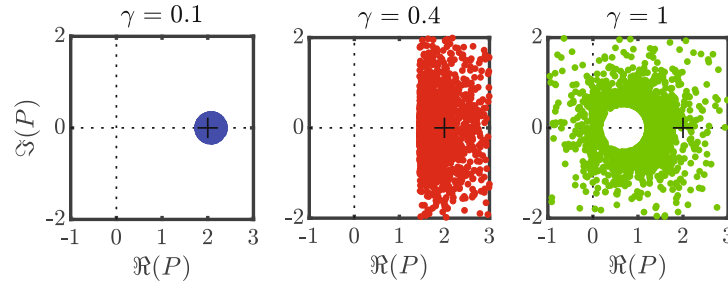

FIGURE 4 Generated candidate dual-Youla-Kučera models $P \in \mathcal{P}^{\text{dY}}$ corresponding to Example 1.

2. For $\gamma = 0.4$, the model set $\mathcal{P}^{\text{dY}}$ is still circularly shaped yet with an infinite radius. Still, the lower bound on the gain is bounded by 1.45, whereas the upper bound has become infinite.

3. For $\gamma = 1$, the candidate models of the dual-Youla-Kučera model set are located everywhere except in a circle of radius 0.5 and centered at 0.7. Indeed, the circles in terms of Δ_u are still mapped onto circles in terms of P, however, the interior of the circles in the Δ_u-plane is mapped onto the exterior of circles into the P-plane.

The particular behavior can be explained by the Möbius transformation. The Möbius transformation is a mapping on the extended complex plane of the form

$$f(z) = \frac{az + b}{cz + d}, \tag{10}$$

where $z \in \mathbb{C}$, and $a, b, c, d \in \mathbb{C}$ satisfy $ad - bc \neq 0$. Observe that in the SISO case, the LFT-based uncertainty structures, (6), are of the form (10). The Möbius transformation can be decomposed into a mapping of elementary sub transformations that are explained in Appendix A. In view of the selected norm-bound γ on the uncertainty Δ_u, the specific interest is in the transformation of a disc in the complex plane hence disc-shaped regions for each frequency. By decomposing the Möbius transformation into elementary transformations in the complex plane, it is immediate that this transformation maps circles into circles in the complex plane. It is emphasized that this encompasses also the results of Example 1. In particular, the dual-Youla-Kučera structure with $\gamma = 0.4$ where a circle of finite radius is mapped into a circle with infinite radius, that is, a line. A consequence of the Möbius transformation is that amplitude and phase bounds can be computed analytically for SISO systems and provides insight into the behavior of these refined uncertainty structures. However, this approach cannot be generalized directly to multivariable systems.

2.3 | Problem formulation

Robust control performance crucially depends on the shape and size of the model set. In particular, the performance guarantee (5) hinges on the selection of the underlying uncertainty structure. Traditionally, model sets for robust control are based on additive or multiplicative uncertainty structures. However, also more refined coprime

factor-based and dual-Youla-Kučera-based uncertainty structures have been developed. As indicated in Section 2.2, dual-Youla-Kučera-based uncertainty structures possess specific advantageous properties compared to traditional uncertainty structures, for example, additive or multiplicative uncertainty structures. In particular, closed-loop performance expressions are affine. However, in contrast to traditional structures, open-loop model characteristics involve general LFT-based expressions. Example 1 confirms that these general LFT-based expressions involve complicated behavior which hampers insight into the underlying open-loop characteristics, and comparison of uncertainty structures.

At the same time, robust control designs are often based on frequency domain-based requirements, for example, loop-shaping-based weighting filters, which underline the importance of frequency domain analysis of the underlying uncertainty structure. An important approach to analyzing and comparing these model sets is to compute bounds on relevant system properties, and the construction of a Bode plot by visualizing frequency-dependent amplitude and phase characteristics. In fact, the Bode plot is a crucial tool in control engineering and provides essential information regarding performance, stability, and robustness.

This paper aims to provide practical insight into the performance and robustness characteristics of uncertainty structures for robust control by providing tools to visualize uncertain multivariable systems and comparing uncertainty structures in a relevant case study. To facilitate comparison, a theoretical analysis and an overview of uncertainty structures are provided in Section 3. In Section 4, the generic method is developed to generate multivariable Bode plots of uncertain multivariable systems. The uncertainty structures introduced in Section 3 are analyzed and compared in an industrial case study in Section 5. In particular, the generic method in Section 4 is employed to generate practical insight into the performance and robustness characteristics of the considered multivariable uncertainty structures. Final, conclusions are provided in Section 6.

3 | IDENTIFICATION-RELATED UNCERTAINTY STRUCTURES FOR ROBUST CONTROL

A key observation is that the robust control performance crucially depends on the considered uncertainty structure. In this section, several uncertainty structures that arise in robust control are introduced, analyzed an compared from a theoretical point of view in their (i) capability to satisfy (3), and (ii) associated worst-case performance in (5). Section 3.6 provides an overview of the comparison and underlines the importance of the development of a generic method for Bode analysis of uncertain multivariable systems. The analysis and comparison in this section are confirmed and extended in a practical case study in Section 5 by employing the generic method for Bode analysis of uncertain multivariable systems in Section 4.

3.1 | Towards theoretical analysis and comparison of uncertainty structures for robusts control

An underlying theoretical framework is essential for the analysis and comparison of uncertainty structures for robust control. From the point of the control goal, the aim is to minimize the upper bound in (5). The closed-loop expression in (5) is complicated, since it depends on the experimental conditions and specific application, and related to this the optimal robust control C^{RP} that follows from synthesis. To further provide a general analysis, in many cases identification is performed in a closed-loop, both from a safety and performance perspective.[6,18,34] Hence, uncertainty is modeled with a given, nonoptimal C^{exp}.

Next, suppose that a certain uncertainty structure is selected that leads to a model set $\mathcal{P}$ such that (3) is satisfied. Then, an approach to compare different model sets is to evaluate their worst-case performance

$$\mathcal{J}_{\text{WC}}(\mathcal{P}, C^{\text{exp}}). \tag{11}$$

The motivation for considering (11) stems from the fact that (4) directly implies the bound

$$\mathcal{J}_{\text{WC}}(\mathcal{P}, C^{\text{RP}}) \leq \mathcal{J}_{\text{WC}}(\mathcal{P}, C^{\text{exp}}). \tag{12}$$

Thus, given two model sets $\mathcal{P}^1$ and $\mathcal{P}^2$, if $\mathcal{J}_{\text{WC}}(\mathcal{P}^1, C^{\text{exp}}) < \mathcal{J}_{\text{WC}}(\mathcal{P}^2, C^{\text{exp}})$, then (12) implies that $\mathcal{P}^1$ has a tighter upper bound compared to $\mathcal{P}^2$ regarding the resulting robust performance. Note that this upper bound does not imply an ordering

in the robust performance as is achieved by $C^{\mathrm{RP}}(\mathcal{P}^1)$ and $C^{\mathrm{RP}}(\mathcal{P}^2)$. However, extensive experimental results, as is also supported by the results in Section 5, reveal that $\mathcal{J}_{\mathrm{WC}}(\mathcal{P}^1, C^{\mathrm{exp}}) < \mathcal{J}_{\mathrm{WC}}(\mathcal{P}^2, C^{\mathrm{exp}})$ typically leads to $\mathcal{J}_{\mathrm{WC}}(\mathcal{P}^1, C^{\mathrm{RP}}(\mathcal{P}^1)) < \mathcal{J}_{\mathrm{WC}}(\mathcal{P}^2, C^{\mathrm{RP}}(\mathcal{P}^2))$.

Furthermore, the minimization of (11) over $\mathcal{P}$, subject to (3), is at the heart of iterative identification and robust control approaches, including.[18,35] An important advantage of criterion (11) is that the robust control design (4) and identification problem (11) may be solved alternately, leading to a monotonously converging iterative procedure.[36] In this paper, the criterion (11) is adopted to evaluate the consequences of the choice of uncertainty structure, see (6), for a pre-specified model $\hat{P}$.

Hence, the performance of the model set, interconnected with C^{exp} follows from the construction of a generalized plant, see Reference 20(Section 3.8)

$$\mathcal{J}_{\mathrm{WC}}(\mathcal{P}, C^{\mathrm{exp}}) = \sup_{\Delta \in \mathbf{\Delta}_u} \|\mathcal{F}_u(\hat{M}, \Delta_u)\|_\infty, \tag{13}$$

where

$$\hat{M}(\hat{H}, C^{\mathrm{exp}}) = \left[\begin{array}{c|c} \hat{M}_{11} & \hat{M}_{12} \\ \hline \hat{M}_{21} & \hat{M}_{22} \end{array} \right]. \tag{14}$$

The matrix $\hat{M}$ in (14) depends on the uncertainty structure $\hat{H}$ (7). In the forthcoming sections, several uncertainty structures in identification for robust control are evaluated in their (i) capability to satisfy (3), and (ii) associated worst-case performance in (11) and (13).

3.2 | Traditional uncertainty structures for robust control

Commonly, (inverse) additive and (inverse) multiplicative uncertainty structures are used in robust controller designs. First, consider a multivariable model set based on additive uncertainty that is given by

$$\mathcal{P}^{\mathrm{Add}} := \{P | P = \hat{P} + \Delta_u, \Delta_u \in \mathbf{\Delta}_u\}, \tag{15}$$

where all considered systems have appropriate dimensions. The corresponding $\hat{H}(\hat{P})$ is given by

$$\hat{H}^{\mathrm{Add}} = \begin{bmatrix} 0 & I \\ I & \hat{P} \end{bmatrix},$$

whereas direct computations reveal that the worst-case performance in (13) is given by

$$\mathcal{J}_{\mathrm{WC}}(\mathcal{P}^{\mathrm{Add}}, C^{\mathrm{exp}}) = \sup_{\Delta_u \in \mathbf{\Delta}_u} \left\| \hat{M}_{22}^{\mathrm{Add}} + \hat{M}_{21}^{\mathrm{Add}} \Delta_u (I - \hat{M}_{11}^{\mathrm{Add}} \Delta_u)^{-1} \hat{M}_{12}^{\mathrm{Add}} \right\|_\infty, \tag{16}$$

for a certain $\hat{M}^{\mathrm{Add}}$, see (14), with in general $\hat{M}_{11}^{\mathrm{Add}} \neq 0$. Hence, the worst-case performance associated with $\mathcal{P}^{\mathrm{Add}}$, see (16), is thus arbitrary and may in fact become unbounded for a bounded $\Delta_u \in \mathbf{\Delta}_u$ due to the inverse in (16). From this perspective, such additive uncertainty structures do not always provide a useful bound in (12). In fact, similar results hold for all uncertainty structures in Reference 4(tab. 9.1), including (inverse) multiplicative structures.

Besides the absence of a finite upper bound in (12), a key shortcoming of additive and multiplicative uncertainty structures involves the fact that the constraint (3) may not hold if such uncertainty structures are used. For instance, from (15) it is immediate that the additive uncertainty structure cannot deal with uncertain *unstable* poles of $\hat{P}$, for example, if P_o is unstable, then for a stable model $\hat{P}$, it holds that $\hat{P} + \Delta_u \in \mathcal{RH}_\infty$, hence (3) cannot be satisfied.

3.3 | Towards coprime-factor based uncertainty structures

To ensure that the constraint in (3) holds for a certain $\mathbf{\Delta}_u$, perturbations on coprime factors can be considered, that is,

$$\mathcal{P}^{\mathrm{CF}} = \left\{ P | P = (\hat{N} + \Delta_N)(\hat{D} + \Delta_D)^{-1}, \left\| \begin{bmatrix} \Delta_N^T & \Delta_D^T \end{bmatrix}^T \right\|_\infty \leq \gamma \right\}, \tag{17}$$

where $\{\hat{N}, \hat{D}\}$ is an RCF of $\hat{P}$. In fact, certain coprime factorizations have a close connection to robustness in the graph and (ν-) gap metric, see Reference 37 and normalized coprime factorizations.[38] Although the guarantee that the constraint (3) is satisfied for at least one $\Delta_u \in \mathcal{RH}_\infty$, such uncertainty structures lead to the general worst-case performance expression in (16). This result follows immediately since if $\hat{P} \in \mathcal{RH}_\infty$, then $\{\hat{P}, I\}$ is an RCF of $\hat{P}$. Hence, the coprime factor uncertainty structure encompasses additive uncertainty as a special case. Summarizing, the key point of coprime factor-based uncertainty is that the true system is guaranteed in the model set, that is, $P_o \in \mathcal{P}^{\mathrm{CF}}$, for some finite overbound γ, however, this does not necessarily lead to a finite bound in the sense of (12).

3.4 | Dual-Youla-Kučera uncertainty structures

To ensure that both the constraint (3) holds and that the bound in (12) is finite, the dual-Youla-Kučera uncertainty structure has been considered in, for example, References 12 and 14. Specifically,

$$\mathcal{P}^{\mathrm{dY}} := \left\{ P \Big| P = \left(\hat{N} + D_c \Delta_u\right) \left(\hat{D} - N_c \Delta_u\right)^{-1}, \Delta_u \in \mathbf{\Delta}_u \right\}, \tag{18}$$

where the pairs $\{\hat{N}, \hat{D}\}$ and $\{N_c, D_c\}$ are *any* RCF of $\hat{P}$ and $C^{\exp}$, respectively. In particular, the model set contains all candidate models that are stabilized by $C^{\exp}$. This means that the bound (12) is always bounded and that a finite bound can always be obtained such that $P_o \in \mathcal{P}^{\mathrm{dY}}$. The model set $\mathcal{P}^{\mathrm{dY}}$ leads to

$$\hat{H}^{\mathrm{dY}} = \left[\begin{array}{c|c} \hat{D}^{-1} N_c & \hat{D}^{-1} \\ \hline D_c + \hat{P} N_c & \hat{P} \end{array} \right]$$

and

$$\hat{M}^{\mathrm{dY}}(\hat{P}, C^{\exp}) = \left[\begin{array}{c|c} 0 & (\hat{D} + C^{\exp}\hat{N})^{-1} \begin{bmatrix} C^{\exp} & I \end{bmatrix} V \\ \hline W \begin{bmatrix} D_c \\ -N_c \end{bmatrix} & WT(\hat{P}, C^{\exp})V \end{array} \right]. \tag{19}$$

Interestingly, (19) can be written as

$$\mathcal{J}_{\mathrm{WC}}(\mathcal{P}^{\mathrm{dY}}, C^{\exp}) = \sup_{\Delta_u \in \mathbf{\Delta}_u} \left\| \hat{M}^{\mathrm{dY}}_{22} + \hat{M}^{\mathrm{dY}}_{21} \Delta_u \hat{M}^{\mathrm{dY}}_{12} \right\|_\infty, \tag{20}$$

which is an affine function of Δ_u and hence bounded for all $\Delta_u \in \mathbf{\Delta}_u$. However, it is emphasized that $\hat{M}^{\mathrm{dY}}_{12}$ and $\hat{M}^{\mathrm{dY}}_{21}$ in (20) are frequency-dependent and multivariable transfer function matrices. Consequently, the bound in (20) and (12) is finite but in general arbitrary. Summarizing, the dual-Youla-Kučera model uncertainty structure, which connects the perturbations on the coprime factors in (17) through the controller $C^{\exp}$, is especially useful from a robust stability perspective since it excludes candidate models that are not stabilized by $C^{\exp}$.

3.5 | Uncertainty structures for achieving robust performance

In Reference 15, a new model uncertainty structure has been presented that has distinct advantages from a robust performance perspective. A key ingredient of this uncertainty structure is a new coprime factorization that arises in a novel connection between control-relevant identification of nominal models and coprime factor identification, extending and providing new insights in earlier results, including.[34] This robust-control-relevant coprime factorization of $\hat{P}$ is given by

$$\begin{bmatrix} \hat{N}^{\mathrm{RCR}} \\ \hat{D}^{\mathrm{RCR}} \end{bmatrix} = \begin{bmatrix} \hat{P} \\ I \end{bmatrix} (\tilde{D}_e + \tilde{N}_{e,2} V_2^{-1} \hat{P})^{-1},$$

where the pair $\left(\begin{bmatrix} \tilde{N}_{e,2} & \tilde{N}_{e,1} \end{bmatrix}, \tilde{D}_e\right)$ is an LCF with co-inner numerator of $C^{\exp}$, see Reference 39. A second ingredient is a certain (W_u, W_y)-normalized RCF. Specifically, the pair $\{N_c^{(W_u, W_y)}, D_c^{(W_u, W_y)}\}$ is a (W_u, W_y)-normalized RCF of C if it is an RCR and, in addition, $(W_u N_c)^* W_u N_c + (W_y D_c)^* W_y D_c = I$, see Reference 15.

Next, by employing the specific robust-control-relevant coprime factorization $\{\hat{N}^{\text{RCR}}, \hat{D}^{\text{RCR}}\}$ of $\hat{P}$ in conjunction with a (W_u, W_y)-normalized RCF of $C^{\exp}$, and (18), a new model set is obtained:

$$\mathcal{P}^{\text{RCR}} := \left\{ P \middle| P = \left(\hat{N}^{\text{RCR}} + D_c^{(W_u, W_y)} \Delta_u\right) \left(\hat{D}^{\text{RCR}} - N_c^{(W_u, W_y)} \Delta_u\right)^{-1}, \Delta_u \in \boldsymbol{\Delta}_u \right\}, \tag{21}$$

The robust-control-relevant model set $\mathcal{P}^{\text{RCR}}$ leads to

$$\hat{H}^{\text{RCR}} = \left[\begin{array}{c|c} (\hat{D}^{\text{RCR}})^{-1} N_c^{(W_u, W_y)} & (\hat{D}^{\text{RCR}})^{-1} \\ \hline D_c^{(W_u, W_y)} + \hat{P} N_c^{(W_u, W_y)} & \hat{P} \end{array} \right]$$

and

$$\hat{M}^{\text{RCR}}(\hat{P}, C^{\exp}) = \left[\begin{array}{c|c} 0 & (\hat{D}^{\text{RCR}} + C^{\exp} \hat{N}^{\text{RCR}})^{-1} \begin{bmatrix} C^{\exp} & I \end{bmatrix} V \\ \hline W \begin{bmatrix} D_c^{(W_u, W_y)} \\ -N_c^{(W_u, W_y)} \end{bmatrix} & W T(\hat{P}, C^{\exp}) V \end{array} \right]. \tag{22}$$

The result (22) leads to a significantly stronger result when compared to (20). Specifically, a main result of Reference 15 reveals that

$$\mathcal{J}_{\text{WC}}(\mathcal{P}^{\text{RCR}}, C^{\exp}) \leq \|\hat{M}_{22}^{\text{RCR}}\|_\infty + \sup_{\Delta_u \in \boldsymbol{\Delta}_u} \|\Delta_u\|_\infty$$
$$= \mathcal{J}(\hat{P}, C^{\exp}) + \gamma, \tag{23}$$

where γ is defined in (9). The robust-control-relevant model uncertainty structure associated with $\mathcal{P}^{\text{RCR}}$ connects the size of model uncertainty and the control criterion. This has significant advantages when compared to alternative model uncertainty structures, including $\mathcal{P}^{\text{Add}}$ and $\mathcal{P}^{\text{RCR}}$. First, the robust-control-relevant model uncertainty structure introduces an appropriate frequency scaling of the model uncertainty channels, hence $\hat{M}_{12}^{\text{RCR}}$ and $\hat{M}_{21}^{\text{RCR}}$ do not appear in (23). Second, the robust-control-relevant model uncertainty structure introduces an appropriate scaling of the model uncertainty channels for multivariable systems by scaling these with respect to the control criterion. Indeed, the scaling of different inputs and outputs is considered important in control system design, see, for example, Reference 20(section 1.4). The appropriate scaling enables the nonconservative use of unstructured model uncertainty, which has significant advantages for certain uncertainty modeling procedures, see, for example, Reference 40, and robust controller synthesis.

3.6 | Comparing uncertainty structures: Overview

Traditional uncertainty structures, for example, additive and multiplicative, typically exhibit affine open-loop characteristics in the uncertainty Δ_u. However, their closed-loop expressions are complicated, that is, involve the general LFT form. As a result, the worst-case performance may become arbitrary or even unbounded indicating that the resulting robust controller may not necessarily achieve a high performance. Besides, an additional drawback of these traditional uncertainty structures is their potential inability to satisfy (3), that is, capture the true system, which is critical to guarantee robust performance.

In sharp contrast to the traditional uncertainty structures, dual-Youla-Kučera uncertainty structures achieve affine closed-loop expressions in the uncertainty Δ_u. Consequently, their worst-case performance may be finite in general. However, the frequency-dependent matrices $\hat{M}_{12}^{\text{dY}}$ and $\hat{M}_{21}^{\text{dY}}$ in (20) lead to an arbitrary worst-case performance indicating that

the resulting robust controller does not necessarily achieve a high performance. In contrast to traditional uncertainty structures, dual-Youla-Kučerauncertainty structures exclude any models that are not stabilized by the controller C^{exp}, which is a considerably useful advantage for achieving robust performance.

The robust-control-relevant uncertainty structure extends to the dual-Youla-Kučerauncertainty structure by employing a specific coprime factorization which provides a finite and useful bound of the worst-case performance (23) which indicates that the resulting robust controller may achieve a high performance. However, in sharp contrast to the traditional uncertainty structures, the open-loop expressions of the dual-Youla-Kučera-based uncertainty structures involve the general form of an LFT and do not reduce to the affine expressions. Although these coprime factor-based uncertainty structures offer significant advantages for robust control, their complicated open-loop characteristics hamper insight into the underlying structure, as shown in Table 1. This underlines the importance of the development of a unified approach for Bode plots of uncertain multivariable systems to gain insight into the underlying uncertainty structure from a robust performance perspective, which is the aim of the following section.

4 | BODE PLOTS OF UNCERTAIN MODEL SETS

In this section, a generic method is developed for Bode analysis, in both (multivariable) magnitude and phase sense, of uncertain multivariable systems. First, suitable measures for multivariable magnitude and phase are introduced. Second, the multivariable magnitude and phase measures are extended to uncertain multivariable systems. Third, an algorithm based on the full-block s-procedure is developed that allows for accurate computation of the multivariable magnitude and phase of uncertain multivariable systems on a frequency-by-frequency basis. The approach applies to general identification-related uncertainty structures, including (6), (15), (17), (18), (21). The proposed generic method for Bode analysis of uncertain multivariable systems constitutes contribution C1.

The general LFT-based structure (6) is used throughout Sections 4.2 and 4.3 to enhance the generality of the results. In addition, to improve generality of the proposed approach, a general uncertainty block based on (8) is considered that may involve highly structured perturbations, for example, References 2 and 41. The unstructured uncertainty perturbation (9) is directly recovered as a special case.

4.1 | Towards multivariable Bode plots of uncertain multivariable systems

4.1.1 | Multivariable magnitude and phase of nominal systems

The Bode plot of a scalar LTI system with the transfer function $P(s) \in \mathcal{R}$ is a graphical representation of the complex frequency response of the system. The Bode plot is a combination of the Bode magnitude and phase plot which are constructed by plotting the magnitude $|P(s)|$ and phase $\arg(P(s))$ on $s = j\omega$ for a grid of frequencies $\omega \in \Omega_d$. The frequency grid Ω_d is defined by the control engineer based on the frequency range of interest and should be sufficiently dense to capture potential resonances. Essentially, the magnitude and phase are based on the polar description of a complex number

$$z = r \exp(j\theta), \tag{24}$$

where $r > 0$ denotes the magnitude and $\theta \in [0, 2\pi)$ denotes the phase. The Bode plot is related to the Nyquist plot through the polar decomposition. In particular, the Nyquist plot is the polar plot of the magnitude and phase for frequencies along the Nyquist D-contour.

The Bode and Nyquist plots are widely used in control engineering for robustness and performance analysis of nominal systems. The close relationship between the polar decomposition, Nyquist plot, and Bode plot is underlined by performance and robustness measures including gain and phase margin.[20]

The key aim of developing a multivariable Bode magnitude and phase plot is to compare uncertainty structures in terms of performance and robustness. Consequently, similar to the Bode plot of SISO systems, a close relationship between the multivariable polar decomposition, the Bode plot, and the Nyquist plot is required. For this reason, analogous to the polar form of a scalar, the polar decomposition of a square system $P(j\omega) \in \mathbb{C}^{n \times n}$ for a fixed frequency $\omega \in \Omega_d$ is defined as Reference 42(section IX.12)

$$P = U H_R, \tag{25}$$

$$P = H_L U, \tag{26}$$

where U is unitary and the matrices H_R and H_L are Hermitian. It is emphasized that the polar decomposition in (25) and (26) holds for a fixed frequency ω and a frequency-by-frequency approach is pursued to generate Bode plots. Further ideas will be developed for a fixed frequency and the frequency dependence is dropped to improve the readability of the results.

Notice that if a SISO system is considered, the multivariable polar decomposition in (25) and (26) reduce the SISO polar decomposition, that is, (24). The matrices U, H_R, and H_L can be determined from the singular value decomposition

$$P = \Phi \Sigma \Psi^*$$

where $U = \Phi \Psi^*$, $H_R = \Psi \Sigma \Psi^*$, and $H_L = \Phi \Sigma \Phi^*$. The multivariable magnitude of P are the eigenvalues of the Hermitian part H_L or H_R of the polar decomposition[42](section IX.12)

$$\sigma(P) = \lambda(H_R) = \lambda(H_L) \geq 0. \tag{27}$$

The multivariable phase based on the multivariable polar decomposition, that is, principal phase,[9] is defined as the arguments of the eigenvalues of the unitary part U

$$\psi(P) = \arg\{\lambda(U)\}. \tag{28}$$

A multivariable Bode plot can be constructed by computing the principal magnitude and phase for each frequency in the frequency grid Ω_d.

4.1.2 | Multivariable magnitude and phase: Interpretation

An important aspect of a Bode plot is its interpretation. A key property of the multivariable magnitude (27) and phase (28) is their relation to robustness analysis. Specifically, the characteristic loci are related to the multivariable magnitude and phase.

Lemma 1. *The magnitude of the eigenvalues of a square system $P \in \mathbb{C}^{n \times n}$ are bounded from above and below by the multivariable magnitude (27)*

$$\underline{\sigma}(P) \leq |\lambda(P)| \leq \overline{\sigma}(P). \tag{29}$$

Proof. The proof is based on Weyl's Theorem, see for example Reference 43. ∎

The relation between the eigenvalues and minimum and maximum singular value, that is, (29), can be used to define an annular region in the complex plane within which the eigenvalues must lie. Next, the relation of the multivariable phase with the eigenvalues is investigated.

Lemma 2. *If the phase spread, that is, the difference between the multivariable phases, is less than π, then, the argument of the eigenvalues of a matrix $P \in \mathbb{C}^{n \times n}$ are bounded from above and below by the multivariable phase (28)*

$$\underline{\psi}(P) \leq \arg\{\lambda(P)\} \leq \overline{\psi}(P) \tag{30}$$

where $\underline{\psi}()$ and $\overline{\psi}()$ denote the minimum and maximum multivariable phase respectively.

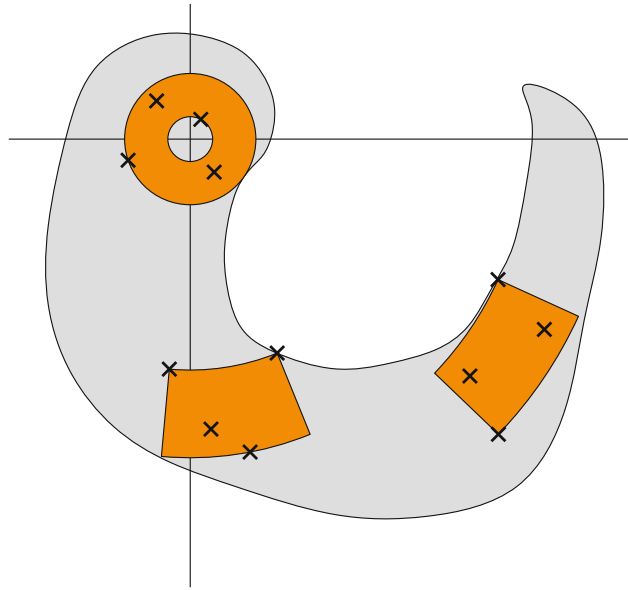*Proof.* A proof is provided in Reference 22(Theorem 2). ∎

FIGURE 5 Illustration of the annular sections defined by the multivariable magnitudes and phases (orange), union of annular sections, that is, principal region (gray), and eigenvalues (black cross).

The minimum and maximum multivariable phase in Lemma 2 can be used to define a cone in the complex plane centered in the origin based on the minimum and maximum phase in (30) within which the eigenvalues of the matrix must lie. Consequently, the combination of Lemma 1 and 2 can be used to span annular sections in the complex plane that contain the eigenvalues as indicated in Figure 5.

If the difference between the minimum and maximum phase, that is, phase spread, is larger than π, then the eigenvalues are contained in an annular region defined by the minimum and maximum singular values. By continuing the analysis along the Nyquist D-contour, a region is drawn within which the characteristic loci must lie, that is, principal region.[22] Application of the generalized Nyquist criterion leads to an alternative Nyquist criterion.[22] Consequently, analogous to the Bode magnitude and phase plot of SISO systems, the multivariable Bode magnitude and phase plot can be used for a wide variety of applications such as stability analysis, robustness analysis, gain margin, phase margin, and performance analysis.

Remark 1. The principal magnitude and phase can be extended to nonsquare systems by adding auxiliary zero columns and rows such that a square system is obtained. In this case, the multivariable magnitude relates to the singular values of the systems which have a clear performance interpretation, that is, minimum and maximum gain of the system. The multivariable phase gets particularly interesting when considering the loop gain which is square by definition. In this case, analogously to the scalar case, the multivariable magnitude has a clear performance interpretation. Since this paper considers robustness and performance properties through visualization, square systems are considered throughout. It is emphasized that the tools presented in this paper can be used for nonsquare systems by adding auxiliary zero columns or rows such that a square system is obtained.

4.2 | Multivariable magnitude and phase of uncertain systems

4.2.1 | Multivariable magnitude

The key idea for the computation of the multivariable magnitude of uncertain systems according to (6) is to compute the minimum and maximum singular value of the uncertain system for each frequency in the frequency grid.

Definition 1. Let $\mathcal{P}$ be an uncertain system according to (6). For a fixed frequency ω the minimum and maximum magnitude are defined as
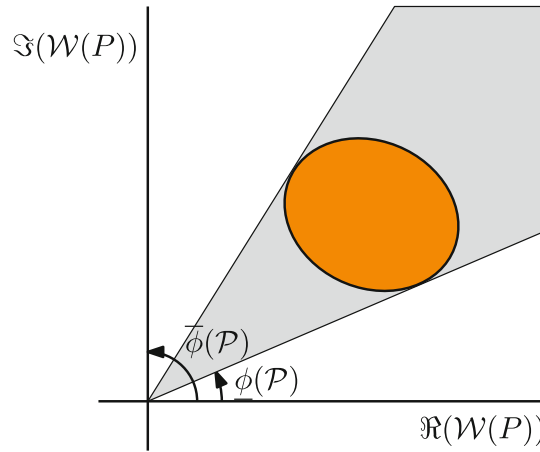
FIGURE 6 Union of numerical ranges $\mathcal{W}(P), \forall P \in \mathcal{P}$ (orange) and cone defined by the multivariable phases $\underline{\phi}(\mathcal{P})$ and $\overline{\phi}(\mathcal{P})$ (grey).

$$\underline{\xi}(\mathcal{P}) = \inf_{P \in \mathcal{P}} \underline{\sigma}\left(P(j\omega)\right), \tag{31}$$

$$\overline{\xi}(\mathcal{P}) = \sup_{P \in \mathcal{P}} \overline{\sigma}\left(P(j\omega)\right). \tag{32}$$

By calculating $\underline{\xi}(\mathcal{P})$ and $\overline{\xi}(\mathcal{P})$ for each frequency in the frequency range of interest, a multivariable Bode magnitude plot is constructed.

4.2.2 | Multivariable phase

In this section, the multivariable phase is defined for uncertain systems, building on the ideas of the principal phase. A direct extension of the principal phase is not immediate, since an explicit expression for the matrix spectrum is not directly available for general complex matrices. For this reason, the numerical range

$$\mathcal{W}(P) = \left\{ x^* P x \middle| x \in \mathbb{C}^n, \|x\| = 1 \right\}$$

is considered, see References 30 and 42 for details. The key benefit of the numerical range is that the set $\mathcal{W}(P)$ is convex. Furthermore, the numerical range is known to contain the spectrum of a matrix.[42] The key idea of using numerical range is to generate a multivariable phase definition that approximates the principal phase of uncertain systems.

To construct a multivariable phase definition of uncertain systems, the numerical range is extended to the uncertain case by considering the union of the numerical ranges $\mathcal{W}(P)$ for $P \in \mathcal{P}$. To define the multivariable phase based on the numerical, consider a cone centered in the origin that contains the union of numerical ranges of the uncertain system $\mathcal{P}$. The cone is described by two angles $\underline{\phi}(\mathcal{P})$ and $\overline{\phi}(\mathcal{P})$ as indicated in Figure 6. The key challenge is to find the smallest cone that contains the union of numerical ranges. The angles $\underline{\phi}(\mathcal{P})$ and $\overline{\phi}(\mathcal{P})$ define the multivariable phase.

Definition 2. Let $\mathcal{P}$ be an uncertain system according to (6). Assume that for a given frequency ω the union of numerical ranges of $\mathcal{P}$ to be in the right half-plane. For a fixed frequency ω the minimum and maximum multivariable phase are defined as

$$\underline{\phi}(\mathcal{P}) = \inf_{P \in \mathcal{P}} \left\{ \inf_{\kappa \in \mathcal{W}(P)} \arg\{\kappa\} \right\}, \tag{33}$$

$$\overline{\phi}(\mathcal{P}) = \sup_{P \in \mathcal{P}} \left\{ \sup_{\kappa \in \mathcal{W}(P)} \arg\{\kappa\} \right\}. \tag{34}$$

Throughout, the numerical range is assumed to be contained in the right half-plane. This assumption is nonrestrictive, since if the numerical range is not in the right half-plane, the system is rotated by an angle v such that $\mathcal{W}(\exp(jv)P(j\omega_0))$ is in the right half-plane for all $P \in \mathcal{P}$.

Remark 2. If the phase spread, that is, the difference between the minimum and maximum phase, is larger than π, the numerical range must contain the origin. Consequently, the phase is contained in a range of 2π.

Remark 3. The multivariable phase based on the numerical range approximates the principal phase. Specifically, the numerical range-based phase bounds the principal phase from below and above

$$\overline{\phi}(P) \geq \psi(P), \qquad \underline{\phi}(P) \leq \psi(P).$$

If the matrix P is normal, then the inequalities become equalities. In this case, the numerical range is the smallest convex set that contains the spectrum of P, that is, $\mathcal{W}(P)$ equals the convex hull of the spectrum of P.[30] Consequently, if a SISO, diagonal, or element-wise system is considered, the numerical range-based phase is exact.

4.2.3 | Element-wise magnitude and phase

Consider the uncertain system $\mathcal{P}$ according to (6). The ij^{th} element of $\mathcal{P}$ is defined as

$$\mathcal{P}_{ij} = \left\{ P_{ij} \middle| P_{ij} \in u_i^* \mathcal{P} u_j \right\}, \tag{35}$$

where u_l denotes a vector of appropriate length with the lth element equal to one and all other elements zero. The multivariable magnitude of Definition 1 and phase of Definition 2 are easily extended to the element-wise case by considering the elements (35). As indicated in Remark 3, the numerical range-based phase is exact with respect to the principal phase in the element-wise case. The element-wise Bode magnitude and phase plot are also valid for nonsquare systems.

4.3 | **Multivariable Bode plots of uncertain systems: Algorithm**

The key step in the development of a magnitude and phase algorithm is to capture the multivariable magnitude and phase in terms of input and output relations. The interconnection in (6) is said to satisfy the quadratic constraint with respect to the performance matrices $\left\{ \Pi_{p,11}, \Pi_{p,12}, \Pi_{p,22} \right\}$ if for every nonzero z, w in (7)

$$\begin{pmatrix} z \\ w \end{pmatrix}^* \begin{pmatrix} \Pi_{p,11} & \Pi_{p,12} \\ \Pi_{p,12}^* & \Pi_{p,22} \end{pmatrix} \begin{pmatrix} z \\ w \end{pmatrix} \prec 0, \tag{36}$$

where the matrices $\Pi_{p,11}, \Pi_{p,12}, \Pi_{p,22} \in \mathbb{H}$ determine the performance characteristics. The performance criterion (36) can be generalized to the IQC framework by including the frequency dependence, see for example Reference 27. However, it is emphasized that a frequency-by-frequency approach is pursued to generate Bode plots. For this reason, the results are developed for a fixed frequency.

Essentially, the performance criterion (36) depends on the uncertainty Δ which makes analysis of (36) not straightforward. The following theorem is an essential result for the performance analysis of uncertain systems.

Theorem 1. *The performance specification (36) holds for all $\Delta \in \mathbf{\Delta}$ if and only if there exist multipliers $\Pi_{p,11}, \Pi_{p,12}, \Pi_{p,22} \in \mathbb{H}$ such that*

$$\begin{pmatrix} \Delta \\ I \end{pmatrix}^* \begin{pmatrix} \Pi_{11} & \Pi_{12} \\ \Pi_{12}^* & \Pi_{22} \end{pmatrix} \begin{pmatrix} \Delta \\ I \end{pmatrix}^* \prec 0 \quad \text{and} \tag{37}$$

$$\begin{pmatrix} \hat{H}_{11} & \hat{H}_{12} \\ I & 0 \\ \hat{H}_{21} & \hat{H}_{22} \\ 0 & I \end{pmatrix}^* \begin{pmatrix} \Pi & 0 \\ 0 & \Pi_p \end{pmatrix} \begin{pmatrix} \hat{H}_{11} & \hat{H}_{12} \\ I & 0 \\ \hat{H}_{21} & \hat{H}_{22} \\ 0 & I \end{pmatrix} \prec 0.$$

Proof. Theorem 1 is based on the full-block s-procedure, see References 44(appendix B) and 45 for a proof. ∎

Theorem 1 provides a necessary and sufficient condition for the uncertain system to satisfy the performance criterion (36). Validating if the uncertain system satisfies the performance criterion is an optimization problem in the matrices Π. However, since (37) needs to hold for all $\Delta \in \mathbf{\Delta}$, the optimization problem is infinite-dimensional. For typical model uncertainty, such as unstructured uncertainty or parameters from a polytope, the matrices $\{\Pi_{11}, \Pi_{12}, \Pi_{22}\}$ are available, for example, in Reference 27. In case unstructured uncertainty is considered, see (9) without any structural constraints, then (37) holds for the matrix

$$\Pi_u = \text{blockdiag}\left(I, -\gamma^2 I\right).$$

For uncertainty structures for which such a multiplier set is not available, the multiplier set can be approximated, see for example, Reference 27. In this case, Theorem 1 provides a sufficient condition.

In the following, the performance criterion (36) and Theorem 1 are used to develop an algorithm to compute the multivariable magnitude and phase.

4.3.1 | Magnitude and phase description

An essential aspect of capturing the magnitude and phase definitions in the quadratic constraint framework (36) is the selection of appropriate performance matrices Π_p. In this section, these performance matrices are derived for the magnitude and phase in Definitions 1 and 2.

Finding the minimum and maximum singular value in Definition 1 can be formulated by computing the largest $\underline{\alpha}$ and smallest $\overline{\alpha}$ such that

$$\underline{\alpha}^2 w^* w - z^* z < 0, \qquad\qquad -\overline{\alpha}^2 w^* w + z^* z \qquad\qquad < 0, \qquad\qquad (38)$$

where w, z refer to the signals in (7).

The parameters $\underline{\alpha}$ and $\overline{\alpha}$ define the interior and exterior respectively, of an annular region in the complex plane. The description of the input-output behavior can be formulated as a quadratic constraint as shown in the following theorem.

Theorem 2. *Let H denote the multivariable system at frequency ω of the form (7) with its input w and output z. The inequalities in (38) hold if and only if (36) holds with the performance matrices*

$$\Pi_{p,1} = \text{blockdiag}\left(-I, \underline{\alpha}^2 I\right), \qquad\qquad \Pi_{p,2} = \text{blockdiag}\left(I, -\overline{\alpha}^2 I\right). \qquad\qquad (39)$$

Proof. Rewriting the inequalities in (38) yields

$$\begin{pmatrix} z \\ w \end{pmatrix}^* \begin{pmatrix} -I & 0 \\ 0 & \underline{\alpha} I \end{pmatrix} \begin{pmatrix} z \\ w \end{pmatrix} < 0, \qquad\qquad (40)$$

$$\begin{pmatrix} z \\ w \end{pmatrix}^* \begin{pmatrix} I & 0 \\ 0 & -\overline{\alpha} I \end{pmatrix} \begin{pmatrix} z \\ w \end{pmatrix} < 0. \qquad\qquad (41)$$

Then, (40) and (41) are equal to (36) with $\Pi_{p,1}$ and $\Pi_{p,2}$. Similarly, consider (36) with $\Pi_{p,1}$ and $\Pi_{p,2}$. Then, (36) with $\Pi_{p,1}$ and $\Pi_{p,2}$ is equivalent to (40) and (41). ∎

The computation of the minimum and maximum phase in Definition 2 can be reformulated by finding the largest $\underline{\beta}$ and smallest $\overline{\beta}$ such that

$$\Re\{w^* z\} > \frac{\Im\{w^* z\}}{\tan(\underline{\beta})}, \qquad\qquad \Re\{w^* z\} < \frac{\Im\{w^* z\}}{\tan(\overline{\beta})}. \qquad\qquad (42)$$

Essentially, the angles $\underline{\beta}$ and $\overline{\beta}$ in (42) define a cone in the complex plane. The largest $\underline{\beta}$ and smallest $\overline{\beta}$ correspond to the multivariable phases in (33) and (34). The inequalities in (42) can be reformulated as a quadratic constraint as follows.

Theorem 3. *Let H denote the multivariable system at frequency ω of the form (7) with its input w and output z. The inequalities in (42) hold if and only if the quadratic constraint (36) holds with the performance matrices*

$$\Pi_{p,3} = \begin{pmatrix} 0 & -\sin(\underline{\beta}) + j\cos(\underline{\beta}) \\ -\sin(\underline{\beta}) - j\cos(\underline{\beta}) & 0 \end{pmatrix}, \tag{43}$$

$$\Pi_{p,4} = \begin{pmatrix} 0 & \sin(\overline{\beta}) - j\cos(\overline{\beta}) \\ \sin(\overline{\beta}) + j\cos(\overline{\beta}) & 0 \end{pmatrix}. \tag{44}$$

Proof. Rewriting the inequalities in (42) yields

$$\begin{pmatrix} z \\ w \end{pmatrix}^* \begin{pmatrix} 0 & -\sin(\underline{\beta}) + j\cos(\underline{\beta}) \\ -\sin(\underline{\beta}) - j\cos(\underline{\beta}) & 0 \end{pmatrix} \begin{pmatrix} z \\ w \end{pmatrix} < 0 \tag{45}$$

$$\begin{pmatrix} z \\ w \end{pmatrix}^* \begin{pmatrix} 0 & \sin(\overline{\beta}) - j\cos(\overline{\beta}) \\ \sin(\overline{\beta}) + j\cos(\overline{\beta}) & 0 \end{pmatrix} \begin{pmatrix} z \\ w \end{pmatrix} < 0. \tag{46}$$

Then, (45) and (46) are equal to (36) with $\Pi_{p,3}$ and $\Pi_{p,4}$. Similarly, consider (36) with $\Pi_{p,3}$ and $\Pi_{p,4}$. Then, (36) with $\Pi_{p,3}$ and $\Pi_{p,4}$ is equivalent to (45) and (46). ∎

Summarizing, Theorem 2 and 3 provide an essential new result for the specific purpose of Bode magnitude and phase plots of uncertain multivariable systems. Specifically, Theorem 2 and 3 build on the general and broadly used framework of quadratic constraints, see for example, Reference 44 and 45. In the next section, Theorems 2 and 3 are used to develop an algorithm to generate Bode plots of uncertain multivariable systems.

4.3.2 | Algorithm

In this section, the results of Theorems 1–3 are embedded in an approach to generate Bode plots of uncertain multivariable systems.

Theorem 4. *Let H be the system of the form (2), $\Delta \in \Delta$ an uncertainty block of the form (9), and consider the fixed bounds $\underline{\alpha}, \overline{\alpha},$ and $\underline{\beta}, \overline{\beta}$. Suppose that (37) holds for the given matrices $\Pi_{11}, \Pi_{12},$ and Π_{22}. The performance matrices $\Pi_{p,i}, i \in \{1, \ldots, 4\}$ are defined by (39), (43), and (44). The matrix inequalities*

$$F(\Pi_{p,i}) = \begin{pmatrix} H_{11} & H_{12} \\ I & 0 \\ H_{21} & H_{22} \\ 0 & I \end{pmatrix}^* \begin{pmatrix} \Pi & 0 \\ 0 & \Pi_{p,i} \end{pmatrix} \begin{pmatrix} H_{11} & H_{12} \\ I & 0 \\ H_{21} & H_{22} \\ 0 & I \end{pmatrix} < 0 \quad \text{for } i \in \{1, \ldots, 4\} \tag{47}$$

hold if and only if

$$\underline{\alpha} \leq \underline{\xi}(\mathcal{P}), \quad \overline{\xi}(\mathcal{P}) \leq \overline{\alpha}, \tag{48}$$

$$\underline{\beta} \leq \underline{\phi}(\mathcal{P}), \quad \overline{\phi}(\mathcal{P}) \leq \overline{\beta}. \tag{49}$$

Proof. Consider the matrix inequality (47) to hold for $\Pi_{p,i}$ with $i \in \{1, \ldots, 4\}$. By virtue of Theorem 1, the performance criterion (36) is satisfied for $\Pi_{p,i}$ with $i \in \{1, \ldots, 4\}$. Application of Theorem 2 and 3 shows that (38) and (42) are satisfied for the bounds $\underline{\alpha}, \overline{\alpha},$ and $\underline{\beta}, \overline{\beta}$ which shows that (48) and (49) hold.

Similarly, consider (48) and (49) to hold for the fixed parameters $\underline{\alpha}$, $\overline{\alpha}$, and $\underline{\beta}$, $\overline{\beta}$. This shows that (38) and (42) are satisfied. By virtue of Theorem 2 and 3, the performance criterion (36) is satisfied for $\Pi_{p,i}$ with $i \in \{1, \ldots, 4\}$. Application of Theorem 1, shows that the matrix inequality (47) holds for $\Pi_{p,i}$ with $i \in \{1, \ldots, 4\}$. ∎

Theorem 4 defines four new feasibility problems for fixed bounds $\underline{\alpha}$, $\overline{\alpha}$, and $\underline{\beta}$ $\overline{\beta}$ for the specific purpose of constructing Bode plots of uncertain multivariable systems that build on the broader framework of quadratic constraints for robust control, see for example, Reference 44. The minimum and maximum magnitude and phase (31), (32), (33), and (34) are determined by solving the following optimization problems

$$\underline{\xi}(\mathcal{P}) = \arg\max_{\underline{\alpha}} \left\{ \underline{\alpha} \middle| F(\Pi_{p,1}(\underline{\alpha})) \prec 0 \right\}, \tag{50}$$

$$\overline{\xi}(\mathcal{P}) = \arg\min_{\overline{\alpha}} \left\{ \overline{\alpha} \middle| F(\Pi_{p,2}(\overline{\alpha})) \prec 0 \right\}, \tag{51}$$

$$\underline{\phi}(\mathcal{P}) = \arg\max_{\underline{\beta}} \left\{ \underline{\beta} \middle| F(\Pi_{p,3}(\underline{\beta})) \prec 0 \right\}, \tag{52}$$

$$\overline{\phi}(\mathcal{P}) = \arg\min_{\overline{\beta}} \left\{ \overline{\beta} \middle| F(\Pi_{p,4}(\overline{\beta})) \prec 0 \right\}. \tag{53}$$

The new optimization problems (50), (51), (52), and (53) allow efficient and reliable computation of the multivariable magnitudes and phases by iterating over the parameters $\underline{\alpha}$, $\overline{\alpha}$ and $\underline{\beta}$, $\overline{\beta}$ through bisection. The optimization problems are convex and allow the magnitude and phase to be determined with user-defined precision. The new algorithm builds on the general framework of linear matrix inequalities and quadratic constraints for robust control for the specific purpose of Bode plots of uncertain multivariable systems and allows reliable computation with general software. The multivariable Bode plot is constructed by computing the magnitude and phase for each frequency in the frequency grid. Consequently, the computations can be executed in parallel. The computational complexity is determined by the number of inputs and outputs, the number of iterations, and the size of the frequency grid.

5 | EXPERIMENTAL COMPARISON BETWEEN IDENTIFICATION-RELATED UNCERTAINTY STRUCTURES FOR ROBUST CONTROL

In this section, the uncertainty structures introduced in Section 3 are analyzed and compared in a case study with the tools provided in Section 4. The uncertainty structures are analyzed in their ability to generate high-performance robust controllers with the visualization tools provided in Section 4. Also, the visualization tools provide insight into the underlying uncertainty structure in view of robust control performance. The uncertainty structures are also tested in their ability to achieve a small worst-case performance bound in the sense of (12) The uncertainty structures are analyzed in their ability to achieve a small worst-case performance. To provide insight into the underlying uncertainty structures, the uncertainty structures are visualized by the tools developed in Section 4. This section constitutes Contribution (C2.1), (C2.2), and (C2.3).

5.1 | Experimental CVT setup

The considered CVT system is depicted in Figure 7. By providing a continuous range of transmission ratios, the CVT 1. potentially reduces fuel consumption in passenger cars by allowing for optimal engine operating conditions, and 2. improves driving comfort.

The main purpose of the CVT is power transmission, where the torque T and angular frequency ω at the primary and secondary shaft are denoted by the subscript p and s, respectively. The torques and angular frequencies of the primary and secondary shafts are related by the transmission ratio. A certain ratio is achieved by applying forces on the sheaves. These forces are directly related to the pressures p_p and p_s in the primary and secondary hydraulic cylinders, respectively, see Figure 7.
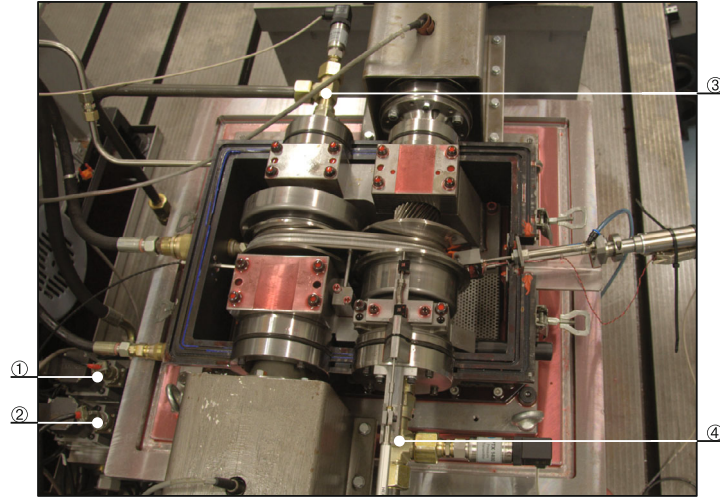
FIGURE 7 Photograph of the experimental CVT system, where ①: primary servo valve, ②: secondary servo valve, ③: pressure measurement p_p at primary hydraulic cylinder, ④: pressure measurement p_s at secondary hydraulic cylinder.

For optimal CVT operation, it is of crucial importance that certain reference pressures are achieved by the closed-loop system. Specifically, in view of the signals in Figure 1, the error

$$e = \begin{bmatrix} e^p \\ e^s \end{bmatrix} = \begin{bmatrix} r_2^p - y^p \\ r_2^s - y^s \end{bmatrix}$$

should be small in some appropriate sense. The measured variables y are given by

$$y = \begin{bmatrix} y_p \\ y_s \end{bmatrix} = \begin{bmatrix} p_p \\ p_s \end{bmatrix}.$$

In addition, the manipulated variables u are given by

$$u = \begin{bmatrix} u_p \\ u_s \end{bmatrix} = \begin{bmatrix} V_p \\ V_s \end{bmatrix},$$

where V_p and V_s are the voltages corresponding to the primary and secondary servo valves, respectively. Throughout, all considered signals and systems evolve in discrete time using a sampling frequency of 1000 [Hz], since all measurements and controller implementations are performed in a digital computer environment.

5.2 | Control goal and nominal model

Throughout this article, it is assumed that weighting filters W and V, see (1), an experimental controller C^{exp}, see Section 3.1, and a nominal model $\hat{P}$, see (6), are given. Specifically, use is made of the loop-shaping-based weighting filters W and V in Reference 46 that are aimed at enhancing CVT performance. Specifically, the weighting filters aim at a bandwidth of 6 [Hz]. In addition, the experimental controller C^{exp} in Reference 46 is employed. Final, in Reference 46, the weighting filters W and V and controller C^{exp} is used to identify a control-relevant parametric model $\hat{P}$, which is internally structured as a robust-control-relevant coprime factorization, that is, $\hat{P} = \hat{N}\hat{D}^{-1}$, see also Section 3.2. Hence, by definition, $\hat{N}, \hat{D} \in \mathcal{RH}_\infty^{2 \times 2}$. In addition, for the specific control-relevant model of the CVT, it turns out that $\hat{P} = \hat{N}\hat{D}^{-1} \in \mathcal{RH}_\infty^{2 \times 2}$. It is emphasized that there are no guarantees with respect to the open-loop stability of the model $\hat{P}$, since it is estimated in a control-relevant manner that enforces closed-loop stability of the interconnection of $\hat{P}$ and C^{exp}.

5.3 | Model uncertainty structures

Three important model structures, in particular, (15), (18), and (21), are compared for clarity of exposition. Note that the additive structure can be used in this application since the nominal model does not contain any open-loop unstable poles, see also Reference 47(tab. 9.1). It is emphasized that in general, additive uncertainty cannot guarantee that the bound in (3) is guaranteed for a finite γ in (9). Furthermore, for each uncertainty structure, the minimum norm-bound to satisfy (3) is different in general, that is, for each model structure $\hat{H}$ in

$$\mathcal{P} = \left\{ P \middle| P = \mathcal{F}_u(\hat{H}(\hat{P}), \Delta_u), \Delta_u \in \mathcal{RH}_\infty^{2\times2}, \|\Delta_u\|_\infty \leq \gamma \right\}, \tag{54}$$

the corresponding γ bound is different. Note that in all three cases, unstructured perturbation models are considered without any additional weighting filters.

First, the additive uncertainty structure can directly be considered using the result in (15). Second, RCFs of $\hat{P}$ and $C^{\exp}$ are required to construct the dual-Youla-Kučera uncertainty structure in (18). Observe that $\hat{P} \in \mathcal{RH}_\infty$, hence the pair $\{\hat{P}, I\}$ is an RCF of $\hat{P}$. Since the controller $C^{\exp}$ contains a pure integrator, $C^{\exp} \neq \mathcal{RH}_\infty$. Hence, $C^{\exp}$ cannot be used directly as a coprime factor. To resolve this, two closed-loop transfer functions are postulated as a coprime factorization for $C^{\exp}$, that is,

$$\begin{bmatrix} N_c \\ D_c \end{bmatrix} = \begin{bmatrix} C^{\exp} \\ I \end{bmatrix} (I + \hat{P}C^{\exp})^{-1} \in \mathcal{RH}_\infty. \tag{55}$$

Clearly, by setting $X = \hat{P}$, $Y = I$, it appears that the Bézout identity $XN + YD = I$ is satisfied. Hence, the pair $\{N_c, D_c\}$ in (55) indeed is an RCF of $C^{\exp}$. Consequently, all RCFs of $C^{\exp}$ are generated by $\{N_cQ_c, D_cQ_c\}$, $Q_c, Q_c^{-1} \in \mathcal{RH}_\infty^{2\times2}$. Note that these RCFs may have a McMillan degree that exceeds the McMillan degree of $\hat{P}$. However, the results that are presented in this paper are independent of the McMillan degrees. Third, the robust-control-relevant model uncertainty structure in (23) is constructed by employing the robust-control-relevant coprime factorization $\hat{P} = \hat{N}\hat{D}^{-1}$ as described in Section 5.2 in conjunction with a (W_u, W_y)-normalized RCF of $C^{\exp}$, which is computed using the state-space results in Reference 35, see Section 3.5.

The required $\mathcal{H}_\infty$-norm bound to satisfy (3) is determined based on local modeling techniques, see Reference 48 for details. The norm bound leads to optimal results in terms of robust-control-relevant model sets.

5.4 | Closed-loop analysis of identification-related model sets

The criterion in (11), that is, $\mathcal{J}_{WC}(\mathcal{P}, C^{\exp})$ is adopted to compare the various model sets. The pursued approach to perform the computations is to perform a sequence of μ-analysis problems, see also Reference 49. In addition, since the considered perturbation structure is μ-simple, see (9) in conjunction with (54), hence the computations, which are based on upper bounds, are exact. The resulting criterion values are given in Table 2.

First, it is observed that $\mathcal{J}_{WC}(\mathcal{P}^{Add}, C^{\exp})$ is unbounded. Hence, the model set contains at least one candidate model that is not stabilized by $C^{\exp}$. By virtue of (11), the model set $\mathcal{P}^{Add}$ does not seem to be a good candidate for robust control

TABLE 2 Comparison of the additive, dual-Youla-Kučera and robust-control-relevant model set.

	$\mathcal{P}^{Add}$	$\mathcal{P}^{dY}$	$\mathcal{P}^{RCR}$
Open-loop uncertain model set	(15)	(18)	(21)
Closed-loop performance bound	(16)	(20)	(23)
γ	1.73	0.55	0.60
$\mathcal{J}(\hat{P}, C^{\exp})$	6.14	6.14	6.14
$\mathcal{J}_{WC}(\mathcal{P}, C^{\exp})$	∞	11.06	6.73
$\min_C \mathcal{J}_{WC}(\mathcal{P}, C)$	3.63	3.20	2.50

design. Second, the controller C^{exp} stabilizes all candidate models in $\mathcal{P}^{\text{dY}}$, which is also reflected by the affine function in (20), hence $\mathcal{J}_{\text{WC}}(\mathcal{P}^{\text{dY}}, C^{\text{exp}})$ indeed is bounded. Specifically, the model set $\mathcal{P}^{\text{dY}}$ leads to a worst-case performance $\mathcal{J}_{\text{WC}}(\mathcal{P}^{\text{dY}}, C^{\text{exp}}) = 11.06$. It is emphasized that this value is arbitrarily large, since it depends on the transfer function matrices $\hat{M}_{12}$ and $\hat{M}_{21}$ in (20), which in turn depend on the arbitrarily chosen coprime factorizations of $\hat{P}$ and C^{exp} in Section 5.3. By virtue of (23), the dual-Youla-Kučera model set has better properties when compared to the additive model set $\mathcal{P}^{\text{Add}}$. Third, the robust-control-relevant model set $\mathcal{P}^{\text{RCR}}$ achieves the smallest worst-case performance, that is, $\mathcal{J}_{\text{WC}}(\mathcal{P}^{\text{RCR}}, C^{\text{exp}}) = 6.73$. In addition, these results confirm that the bound (23) holds and is tight.

5.5 | Open-loop analysis of identification-related model sets

The properties of Dual-Youla-Kučera-based uncertainty structures, as compared to traditional uncertainty structures such as the additive uncertainty structure, have been studied in Section 3.1 and Example 1. One notable advantage of the Dual-Youla-Kučera-based structures is that their closed-loop expressions are affine, which simplifies their analysis. However, as seen in Example 1, the open-loop model characteristics of these structures involve general LFT-based expressions that make it difficult to gain insight into the underlying uncertainty structure and to compare different uncertainty structures.

To address this issue, this section aims to provide more in-depth insight into the underlying uncertainty structures, investigate their implications for robust control design, and compare model sets by visualizing their open-loop characteristics using the tools developed in Section 4. Specifically, the model sets are compared using both the multivariable and element-wise Bode plots (Figures 8 and 9).

First, it is observed that the additive model set $\mathcal{P}^{\text{Add}}$ leads to a finite multivariable magnitude in the multivariable Bode magnitude plot (Figure 8). Also, the multivariable Bode plot indicates that there exist singular values of $\mathcal{P}^{\text{Add}}$ equal to zero over the complete frequency range. As a consequence, the numerical range contains the origin which leads to a multivariable phase in the range $[0, 2\pi]$ in the multivariable phase plot, see also Remark 2. The multivariable magnitude plot of the robust-control-relevant model set $\mathcal{P}^{\text{RCR}}$ leads to an infinite magnitude in the low- and high-frequency range. The model quality at these frequencies typically does not influence the control performance, see also Reference 9. In contrast, around the desired bandwidth of 6 [Hz], see Section 5.2, the robust-control-relevant model set $\mathcal{P}^{\text{RCR}}$ is tight and hence the uncertainty is small. Thus, the multivariable Bode magnitude and phase plots reveal that the robust-control-relevant model set is significantly smaller in the frequency range that is important for control, that is, the target bandwidth, compared to the additive model set.

Second, it is observed that in the elements in the element-wise Bode plot (Figure 9), the additive model set $\mathcal{P}^{\text{Add}}$ leads to a relatively small uncertainty in the low-frequency range. In contrast, the robust-control-relevant model set $\mathcal{P}^{\text{RCR}}$ leads to infinitely large uncertainty in the low-frequency range. This effect is attributed to the control-relevant coprime factors.

Third, it is observed that the tightness of the two model sets around the desired bandwidth of 6 Hz is different for both the multivariable and element-wise Bode plots. Specifically, it is noted that $\mathcal{P}^{\text{RCR}}$ is highly accurate in this frequency range, resulting in small uncertainties in all element-wise transfer functions. However, the same cannot be said for $\mathcal{P}^{\text{Add}}$, which exhibits significantly more uncertainty in this range, especially for the P_{22}, P_{21}, and P_{P12} elements. This high uncertainty is associated with an inappropriate scaling of the uncertainty channels which may result in a conservative robust control design. In contrast, $\mathcal{P}^{\text{RCR}}$ leads to optimal scaling of uncertainty channels from a control perspective, as shown in (23).

Fourth, in both cases, $\mathcal{P}^{\text{RCR}}$ and $\mathcal{P}^{\text{Add}}$ exhibit large uncertainty at high frequencies. However, the effect of this uncertainty is different for the two model sets. For $\mathcal{P}^{\text{RCR}}$, the model quality at higher frequencies typically does not affect control performance, see also Reference 9. However, for $\mathcal{P}^{\text{Add}}$, the gain of the open-loop model $\hat{P}$ is significantly smaller at higher frequencies, which implies that the model uncertainty generally has a larger relative effect. This behavior is a concern from a control perspective, as it may lead to a conservative robust control design.

For the sake of completeness, the model set $\mathcal{P}^{\text{dY}}$ is also visualized and compared, see Figures 8 and 9. The most important difference between $\mathcal{P}^{\text{Add}}$ and $\mathcal{P}^{\text{dY}}$ involves the fact that the former model set contains at least one candidate model that is not stabilized by C^{exp}, whereas the latter model set only contains candidate models that are stabilized by C^{exp} and, in addition, achieve a performance that is bounded by 11.06, see Table 2.

When comparing $\mathcal{P}^{\text{dY}}$ and $\mathcal{P}^{\text{RCR}}$ using the multivariable magnitude and phase Bode plots, it is clear that the $\mathcal{P}^{\text{dY}}$ is significantly larger compared to $\mathcal{P}^{\text{RCR}}$. Interestingly, Table 2 reveals that the size of the uncertainty γ is of comparable size for both model sets. This indicates that the scaling of the uncertainty channels of the robust-control-relevant model set is better compared to the dual-Youla-Kučera model set.
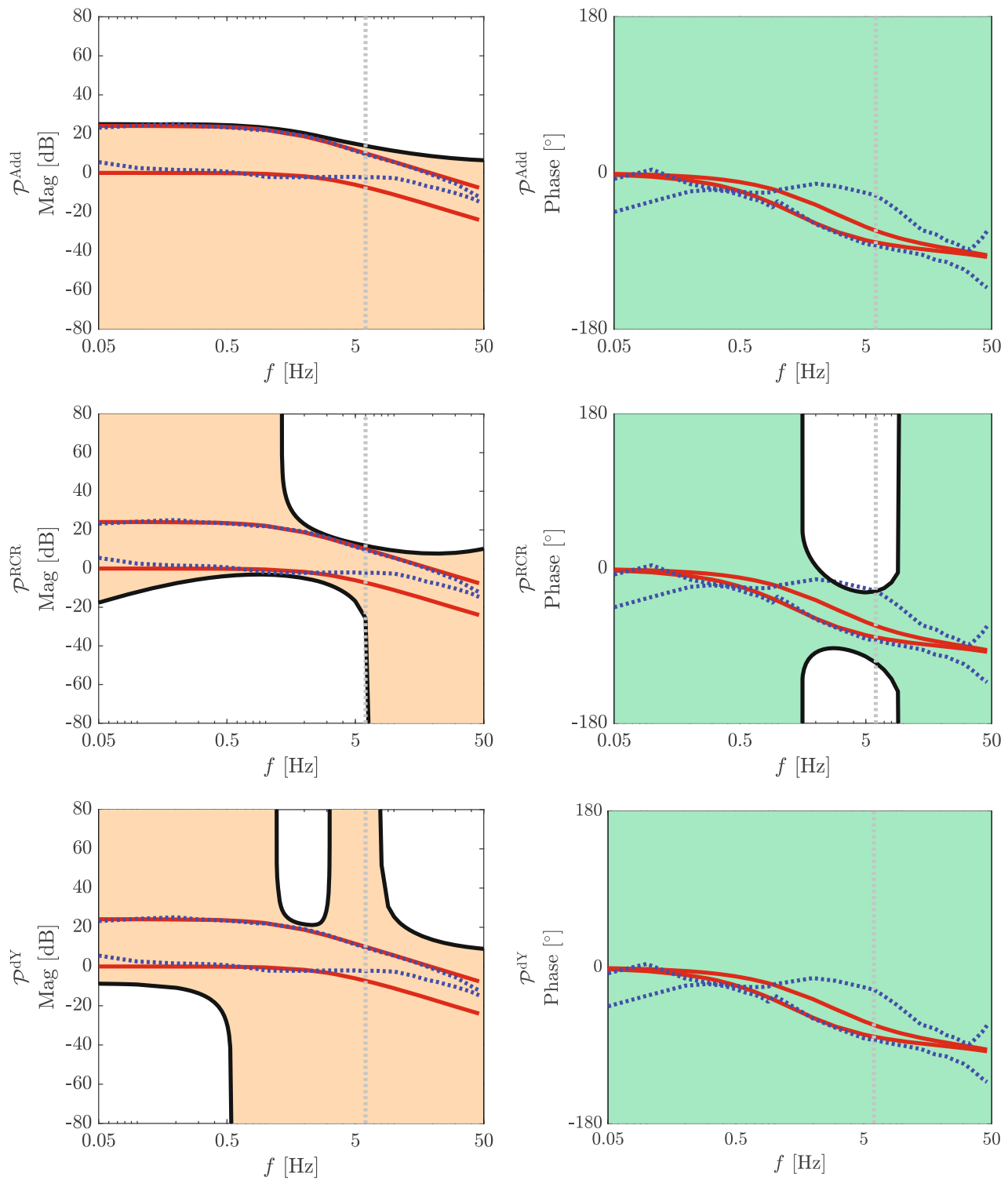
FIGURE 8 Multivariable Bode magnitude (left, orange) and phase (right, green) of the additive model set (top), robust-control-relevant model set (center), and dual-Youla-Kučera model set (bottom). Also depicted are the nominal model $\hat{P}$ (solid red) and the frequency response function $\widetilde{P}_o(\omega_i), \omega_i \in \Omega^{\text{id}}$ (blue dots) based on (27) and (28). The target bandwidth is indicated by the grey dotted line. The nominal model is identical for each model structure, and the size of the uncertainty depends on the considered model set.
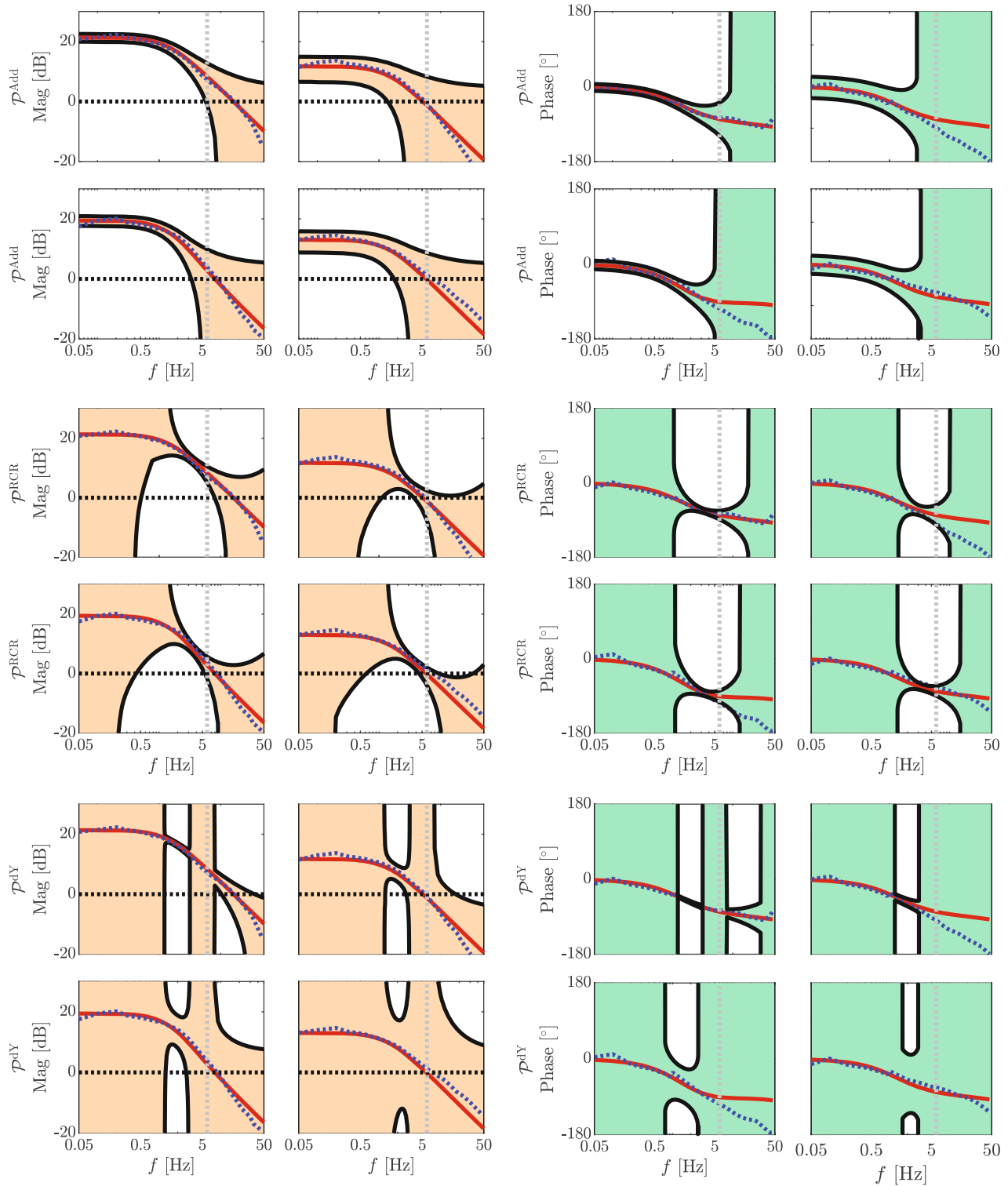
FIGURE 9 Element-wise Bode magnitude (left, orange) and phase (right, green) of the additive model set (top), robust-control-relevant model set (center), and dual-Youla-Kučera model set (bottom). Also depicted are the nominal model $\hat{P}$ (solid red), the frequency response function $\widetilde{P}_o(\omega_i)$, $\omega_i \in \Omega^{\mathrm{id}}$ (blue dots), and the target bandwidth (grey dotted). The nominal model is identical for each model structure, and the size of the uncertainty depends on the considered model set.

Similarly, when comparing $\mathcal{P}^{\text{dY}}$ and $\mathcal{P}^{\text{RCR}}$ using the element-wise Bode plots, it appears that the scaling of the uncertainty channels of the model set $\mathcal{P}^{\text{RCR}}$ indeed is better than $\mathcal{P}^{\text{dY}}$. Specifically, around 1 [Hz], the model set $\mathcal{P}^{\text{dY}}$ shows a very small uncertainty in the transfer function $u^p \mapsto p^p$, whereas the transfer function $u^s \mapsto p^s$ is highly uncertain. In contrast, the uncertainty associated with $\mathcal{P}^{\text{RCR}}$ in the same frequency region is of comparable size for the different transfer functions in Figure 9. This confirms that the robust-control-relevant uncertainty structure appropriately scales the uncertainty channels with respect to the control criterion.

5.6 | Robust controller synthesis

The model sets $\mathcal{P}$ and $\mathcal{P}^{\text{Add}}$ are further investigated through a robust controller synthesis. Note that the bound in (5) holds for each of the model sets in Section 5.3. However, no explicit statements can be made regarding the ordering of the resulting controllers in terms of worst-case performance.

First, consider the controller

$$C^{\text{RCR}} = \arg \min_C \mathcal{J}_{\text{WC}}(\mathcal{P}^{\text{RCR}}, C)$$

that provides the performance guarantees

$$\mathcal{J}(P_o, C^{\text{RCR}}) \le \mathcal{J}_{\text{WC}}(\mathcal{P}^{\text{RCR}}, C^{\text{RCR}}) \le \mathcal{J}_{\text{WC}}(\mathcal{P}^{\text{RCR}}, C^{\text{exp}}) = 6.73.$$

Indeed, the controller C^{RCR} leads to

$$\mathcal{J}_{\text{WC}}(\mathcal{P}^{\text{RCR}}, C^{\text{RCR}}) = 2.50.$$

Second, recall that the additive model set $\mathcal{P}^{\text{Add}}$ leads to an infinite worst-case when evaluated for C^{exp}, see Table 2, since the model set is not robustly stable under closed-loop with C^{exp} implemented. Since the model set $\mathcal{P}^{\text{Add}}$ is open-loop stable, clearly a controller exists that simultaneously stabilizes all candidate models in $\mathcal{P}^{\text{Add}}$. In fact, $C = 0$ is such a stabilizing controller. Hence,

$$C^{\text{Add}} = \arg \min_C \mathcal{J}_{\text{WC}}(\mathcal{P}^{\text{Add}}, C)$$

always leads to a bounded worst-case performance. However, the worst-case performance is arbitrary, since $\mathcal{J}_{\text{WC}}(\mathcal{P}^{\text{Add}}, C^{\text{exp}})$ is unbounded. Analysis of the optimal controller C^{Add} leads to

$$\mathcal{J}_{\text{WC}}(\mathcal{P}^{\text{Add}}, C^{\text{Add}}) = 3.63.$$

For this specific situation, the controller C^{Add} achieves a reasonably good performance. It is emphasized that this is to a large extent attributed to the favorable scaling and specific properties of the open-loop model $\hat{P}$. In general, $\mathcal{J}_{\text{WC}}(\mathcal{P}^{\text{Add}}, C^{\text{Add}})$ may be significantly worse than $\mathcal{J}_{\text{WC}}(\mathcal{P}^{\text{RCR}}, C^{\text{exp}})$.

Third, the controller

$$C^{\text{dY}} = \arg \min_C \mathcal{J}_{\text{WC}}(\mathcal{P}^{\text{dY}}, C)$$

is computed, leading to

$$\mathcal{J}_{\text{WC}}(\mathcal{P}^{\text{dY}}, C^{\text{dY}}) = 3.20.$$

Interestingly, the ordering of $\mathcal{P}^{\text{Add}}$, $\mathcal{P}^{\text{dY}}$, and $\mathcal{P}^{\text{RCR}}$ in terms of $\mathcal{J}_{\text{WC}}(\mathcal{P}, C^{\text{exp}})$, that is,

$$\mathcal{J}_{\text{WC}}(\mathcal{P}^{\text{Add}}, C^{\text{exp}}) \ge \mathcal{J}_{\text{WC}}(\mathcal{P}^{\text{dY}}, C^{\text{exp}}) \ge \mathcal{J}_{\text{WC}}(\mathcal{P}^{\text{RCR}}, C^{\text{exp}}) \tag{56}$$
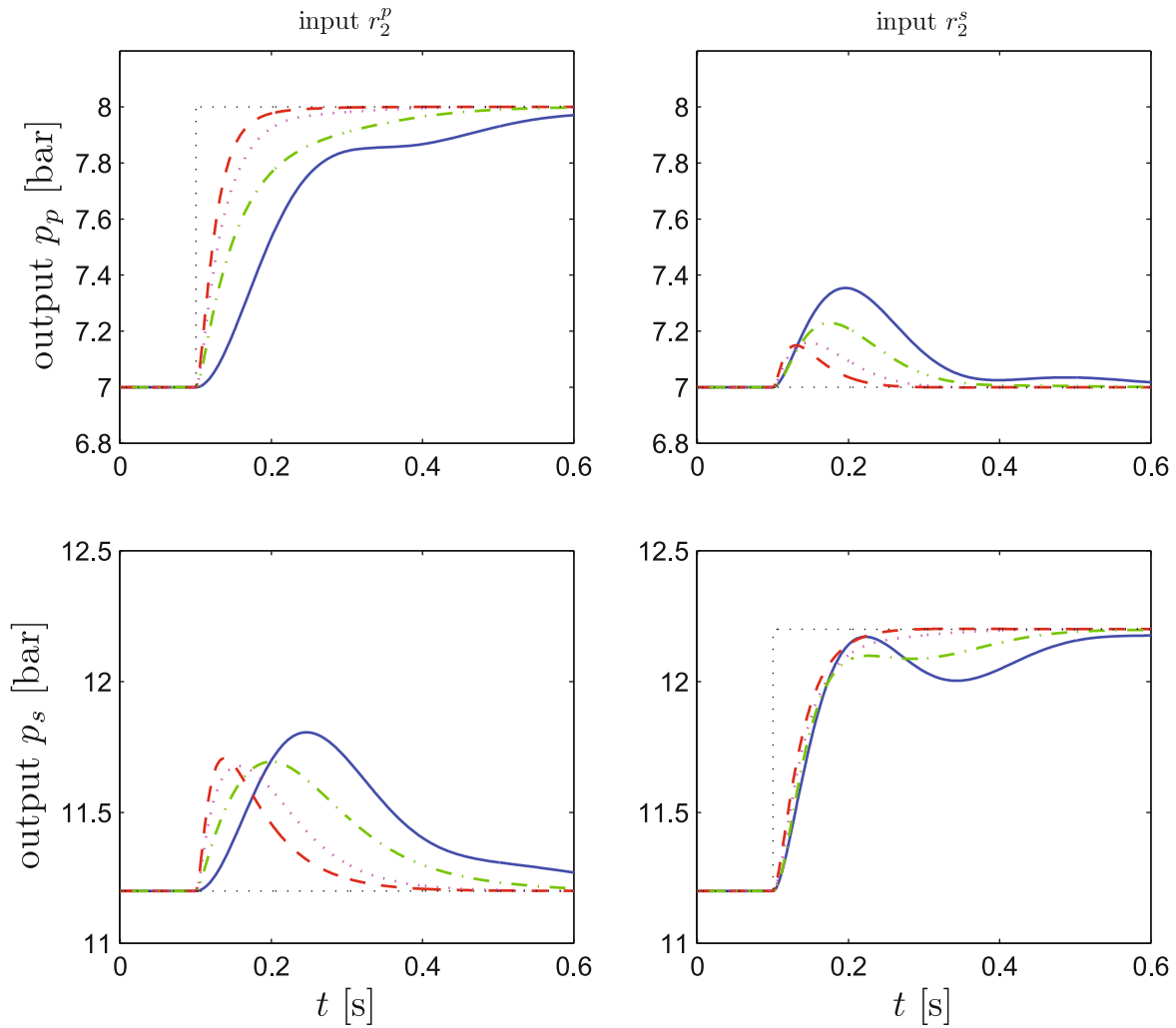
FIGURE 10 Closed-loop step responses ($r_2 \mapsto y$): initial controller C^{exp} (solid blue), optimal robust controller C^{RCR} (dashed red), optimal robust controller C^{Add} (dash-dotted green), optimal robust controller C^{dY} (dotted).

corresponds to an identical ordering in terms of the optimal robust controllers C^{Add}, C^{dY}, and C^{RCR} that are based on these model sets, that is,

$$\mathcal{J}_{\text{WC}}(\mathcal{P}^{\text{Add}}, C^{\text{Add}}) \geq \mathcal{J}_{\text{WC}}(\mathcal{P}^{\text{dY}}, C^{\text{dY}}) \geq \mathcal{J}_{\text{WC}}(\mathcal{P}^{\text{RCR}}, C^{\text{RCR}}). \tag{57}$$

It is emphasized that the ordering in (56) and (57) typically arises in robust controller synthesis, but is not guaranteed.

Final, the resulting controllers are implemented on the nominal model $\hat{P}$, see Section 5.2. The resulting step responses in Figure 10 confirm that a reduced worst-case leads to a faster response in terms of settling time and less interaction, hence improved performance.

6 | CONCLUSIONS

The selection of uncertainty structures is a crucial step in system identification for robust control. The trend toward multivariable systems and more complicated uncertainty structures complicates comparison, insight, and analysis of robustness and performance. This paper compares several uncertainty structures that arise in system identification for robust control. To facilitate comparison and analysis of uncertain model sets for robust control, a new approach is presented which allows the generation of element-wise and multivariable Bode magnitude and phase plots of uncertain systems. The considered multivariable magnitude and phase intuitively connect to well-known concepts for performance

and robustness, for example, gain and phase margin. The case study illustrates the effectiveness of the proposed approach by indicating through visualization how the shape and size of model structures influence the resulting robust control performance.

DATA AVAILABILITY STATEMENT

The experimental data is not shared.

ORCID

Paul Tacx 🄳 https://orcid.org/0000-0002-5707-7709

REFERENCES

1. Oomen T. Advanced motion control for precision mechatronics: Control, identification, and learning of complex systems. *IEEJ J Ind Appl.* 2018;7(2):127-140.
2. van de Wal M, van Baars G, Sperling F, Bosgra O. Multivariable $\mathscr{H}_\infty/\mu$ feedback control design for high-precision wafer stage motion. *Control Eng Pract.* 2002;10(7):739-755.
3. Hjalmarsson H, Gunnarsson S, Gevers M. Optimality and sub-optimality of iterative identification and control design schemes. *Proceedings of the 1995 American Control Conference. Seattle, WA, USA.* IEEE; 1995:2559-2563.
4. Zhou K, Doyle JC. *Essentials of Robust Control.* Prentice hall; 1998:104.
5. Bhattacharyya SP, Keel LH. *Robust Control: The Parametric Approach.* Pergamon; 1995.
6. Gevers M, Bombois X, Codrons B, Scorletti G, Anderson BDO. Model validation for control and controller validation in a prediction error identification framework–Part I: Theory. *Automatica.* 2003;39(3):403-415.
7. Biannic JM, Roos C, Bennani S, Boquet F, Preda V, Girouart B. Advanced probabilistic μ-analysis techniques for AOCS validation. *Eur J Control.* 2021;62:120-129.
8. Doyle JC. A review of μ for case studies in robust control. *IFAC Proc Vol.* 1987;20(5):365-372.
9. McFarlane DC, Glover K. *Robust Controller Design Using Normalized Coprime Factor Plant Descriptions.* Springer; 1990.
10. Lanzon A, Papageorgiou G. Distance measures for uncertain linear systems: A general theory. *IEEE Trans Autom Control.* 2009;54(7):1532-1547.
11. Ma CCH. Comments on" A necessary and sufficient condition for stability of a perturbed system" by Q. Huang and R. Liu. *IEEE Trans Autom Control.* 1988;33(8):796-797.
12. Anderson BDO, James MR, Limebeer DJ. Robust stabilization of nonlinear systems via normalized coprime factor representations. *Automatica.* 1998;34(12):1593-1599.
13. Niemann H. Dual Youla parameterisation. *IEE Proc Control Theory Appl.* 2003;150(5):493-497.
14. Douma SG, van den Hof PMJ. Relations between uncertainty structures in identification for robust control. *Automatica.* 2005;41(3):439-457.
15. Oomen T, Bosgra O. System identification for achieving robust performance. *Automatica.* 2012;48(9):1975-1987.
16. Boeren F, Lanzon A, Oomen T. Iterative identification and control using non-normalized coprime factors with application in wafer stage motion control. *IEEE Trans Control Syst Technol.* 2018;28(2):413-424.
17. Jung M, Glover K, Christen U. Comparison of uncertainty parameterisations for $\mathscr{H}_\infty$ robust control of turbocharged diesel engines. *Control Eng Pract.* 2005;13(1):15-25.
18. de Callafon RA, van den Hof PMJ. Suboptimal feedback control by a scheme of iterative identification and control design. *Math Modell Syst.* 1997;3(1):77-101.
19. Bayard DS, Chiang RY. Identification, uncertainty characterization and robust control synthesis applied to large flexible structures control. *Int J Robust Nonlinear Control.* 1998;8(2):97-112.
20. Skogestad S, Postlethwaite I. *Multivariable Feedback Control: Analysis and Design.* Wiley; 2007:2.
21. James HM, Nichols NB, Phillips RS. *Theory of Servomechanisms.* McGraw-Hill New York; 1947:25.
22. Postlethwaite I, Edmunds J, MacFarlane A. Principal gains and principal phases in the analysis of linear multivariable feedback systems. *IEEE Trans Autom Control.* 1981;26(1):32-46.

23. Pavlov A, van de Wouw N, Nijmeijer H. Frequency response functions for nonlinear convergent systems. *IEEE Trans Autom Control*. 2007;52(6):1159-1165.

24. Oomen T, van de Wal M, Bosgra O. Design framework for high-performance optimal sampled-data control with application to a wafer stage. *Int J Control*. 2007;80(6):919-934.

25. Gantmakher FR. *The Theory of Matrices*. American Mathematical Society; 1959:131.

26. Oomen T, Quist S, van Herpen R, Bosgra O. Identification and visualization of robust-control-relevant model sets with application to an industrial wafer stage. *49th IEEE Conference on Decision and Control (CDC). Atlanta, GA, USA*. IEEE; 2010:5530-5535.

27. Megretski A, Rantzer A. System analysis via integral quadratic constraints. *IEEE Trans Autom Control*. 1997;42(6):819-830.

28. Tits AL, Balakrishnan V, Lee L. Robustness under bounded uncertainty with phase information. *IEEE Trans Autom Control*. 1999;44(1):50-65.

29. Laib K, Korniienko A, Dinh M, Scorletti G, Morel F. Hierarchical robust performance analysis of uncertain large scale systems. *IEEE Trans Autom Control*. 2017;63(7):2075-2090.

30. Owens DH. *The Numerical Range: A Tool for Robust Stability Studies*. Dept. of Automatic Control and System Engineering; 1984.

31. Tacx P, Oomen T. Bode Analysis of Uncertain Multivariable Systems. *Proceedings of the 2022 American Control Conference. Atlanta, GA, USA*. IEEE.; 2022:5056-5061.

32. McFarlane D, Glover K. A loop-shaping design procedure using H_∞ synthesis. *IEEE Trans Autom Control*. 1992;37(6):759-769.

33. Dullerud GE, Paganini F. *A Course in Robust Control Theory: A Convex Approach*. Springer Science & Business Media; 2013:36.

34. Schrama RJP. Accurate identification for control: The necessity of an iterative scheme. *IEEE Trans Autom Control*. 1992;37(7):991-994.

35. Oomen T, van Herpen R, Quist S, van de Wal M, Bosgra O, Steinbuch M. Connecting system identification and robust control for next-generation motion control of a wafer stage. *IEEE Trans Control Syst Technol*. 2013;22(1):102-118.

36. Bayard D, Yam Y, Mettler E. A criterion for joint optimization of identification and robust control. *IEEE Trans Autom Control*. 1992;37(7):986-991.

37. Georgiou TT, Smith MC. Optimal robustness in the gap metric. *Proceedings of the 1989 Conference on Decision and Control. Tampa, FL, USA*. IEEE.; 1989:2331-2336.

38. Vinnicombe G. *Uncertainty and Feedback: $\mathscr{H}_\infty$ Loop-shaping and the ν-gap Metric*. World Scientific; 2001.

39. Smith RS, Chu CC, Fanson JL. The design of H_∞ controllers for an experimental non-collocated flexible structure problem. *IEEE Trans Control Syst Technol*. 1994;2(2):101-109.

40. Toker O, Chen J. On computational complexity of invalidating structured uncertainty models. *Syst Control Lett*. 1998;33(3):199-207.

41. de Callafon RA, van den Hof PMJ. Multivariable feedback relevant system identification of a wafer stepper system. *IEEE Trans Control Syst Technol*. 2001;9(2):381-390.

42. Gantmacher F. *The theory of matrices*. Chelsea Publishing; 1964.

43. Weyl H. Inequalities between the two kinds of eigenvalues of a linear transformation. *Proc Natl Acad Sci*. 1949;35(7):408-411.

44. Scherer CW. LPV control and full block multipliers. *Automatica*. 2001;37(3):361-375.

45. Scherer CW. A full block S-procedure with applications. *Proceedings of the 1997 Conference on Decision and Control. San Diego, CA, USA*. IEEE.; 1997:3, 2602-2607.

46. Oomen T, van der Meulen S, Bosgra O, Steinbuch M, Elfring J. A robust-control-relevant model validation approach for continuously variable transmission control. *Proceedings of the 2010 American Control Conference. Baltimore, MD, USA*. IEEE.; 2010:3518-3523.

47. Zhou K, Doyle J, Glover K. Robust and optimal control. *Control Eng Pract*. 1996;4(8):1189-1190.

48. Tacx P, Oomen T. Accurate $\mathscr{H}_\infty$-norm estimation via finite-frequency norms of local parametric models. *Proceedings of the 2021 American Control Conference. New Orleans, LA, USA*. IEEE.; 2021:332-337.

49. Fan MK, Tits A. A measure of worst-case H_∞ performance and of largest acceptable uncertainty. *Syst Control Lett*. 1992;18(6):409-421.

APPENDIX A. MÖBIUS TRANSFORMATION

The Möbius transformation (10) consists of five elementary subtransformations

$$f(z) = f_5 \circ f_4 \circ f_3 \circ f_2 \circ f_1(z). \tag{A1}$$

The five elementary transformations are defined and explained below.

- $A = f_1(z) = \frac{1}{z}$. Consider a circle with a radius r

$$z = \exp(i\theta), \quad \theta = [0, 2\pi).$$

Applying $f_1(z)$ yields

$$A = f_1(z) = \frac{1}{r}\exp(-i\theta), \quad \theta = [0, 2\pi]. \tag{A2}$$

The result reveals that the interior of the circle with the radius r is mapped to the exterior of a circle with radius $\frac{1}{r}$.

- $B = f_2(A) = A + \frac{c}{d}$. The mapping $f_2(A)$ is clearly a translation by the complex number $\frac{c}{d}$. Applying the transformation (A2) yields

$$B = f_2(A) = \frac{1}{r}\exp(-i\theta) + \frac{c}{d}.$$

hence the center of the circle is moved away from the origin by the complex number $\frac{c}{d}$.

- $C = f_3(B) = \frac{1}{B}$. The mapping $f_3(B)$ is, similar to $f_1(z)$, an inversion. However, in case circles are considered, the center of the circle need not be the origin due to the transformation $f_2(A)$. To appropriately handle this case, it is convenient to parameterize the circle in Cartesian coordinates, that is,

$$\left(\mathfrak{R}(B) - \mathfrak{R}\left(\frac{c}{d}\right)\right)^2 + \left(\mathfrak{I}(B) - \mathfrak{I}\left(\frac{c}{d}\right)\right)^2 = \frac{1}{r^2}. \tag{A3}$$

Observe that $C = \frac{1}{B}$ and reformulating (A3) yields

$$\left(\mathfrak{R}(C) - \frac{\mathfrak{R}(\frac{c}{d})r^2}{\left|\frac{c}{d}\right|r^2 - 1}\right)^2 + \left(\mathfrak{I}(C) - \frac{\mathfrak{I}(\frac{c}{d})r^2}{\left|\frac{c}{d}\right|^2 r^2 - 1}\right)^2 = \left(\frac{r}{\left|\frac{c}{d}\right|^2 r^2 - 1}\right)^2. \tag{A4}$$

Clearly, (A4) describes circles in case $\left|\frac{c}{d}\right| \neq r^2$. In contrast, in case $\left|\frac{c}{d}\right| = r^2$, (A4) describes a line, which can be interpreted as a circle with an infinite radius.

The main interpretation of (A4) is as follows. In case $\left|\frac{b}{d}\right|^2 > \frac{1}{r^2}$, then the exterior of the circle is mapped onto the exterior. In case $\left|\frac{b}{d}\right|^2 = \frac{1}{r^2}$, then the exterior of the circle is mapped onto a half-plane. Final, if $\left|\frac{b}{d}\right|^2 = \frac{1}{r^2}$, then the exterior of the circle is mapped onto the interior.

- $D = f_4(C) = \frac{ad-bc}{d^2}C$. The mapping $f_4(C)$ is a homothety and rotation. Let

$$\alpha\exp(i\theta) = \frac{ad - bc}{d^2}$$

be the polar representation of the constant $\frac{ad-bc}{d^2}$. Applying the transformation to (A4) leads to a new circle parameterized by

$$\left(\mathfrak{R}(C) - \frac{\mathfrak{R}(\frac{c}{d})r^2}{\left|\frac{c}{d}\right|r^2 - 1}\alpha\cos\alpha\right)^2 + \left(\mathfrak{I}(C) - \frac{\mathfrak{I}(\frac{c}{d})r^2}{\left|\frac{c}{d}\right|^2 r^2 - 1}\alpha\sin\alpha\right)^2 = \left(\frac{\alpha r}{\left|\frac{c}{d}\right|^2 r^2 - 1}\right)^2. \tag{A5}$$

- $E = f_5(D) = D + \frac{b}{d}$. Similar to the elementary transformation $f_3(B)$, the mapping $f_5(D)$ is a transformation by the complex number $\frac{b}{d}$. Applying the transformation to (A5) leads to a new circle parameterized by

$$\left(\mathfrak{R}(C) - \frac{\mathfrak{R}(\frac{c}{d})r^2}{\left|\frac{c}{d}\right|r^2 - 1}\alpha\cos\alpha - \mathfrak{R}\left(\frac{b}{d}\right)\right)^2 + \left(\mathfrak{I}(C) - \frac{\mathfrak{I}(\frac{c}{d})r^2}{\left|\frac{c}{d}\right|^2 r^2 - 1}\alpha\sin\alpha - \mathfrak{I}\left(\frac{b}{d}\right)\right)^2 = \left(\frac{\alpha r}{\left|\frac{c}{d}\right|^2 r^2 - 1}\right)^2.$$

Summarizing, from the composition of the elementary mappings, see (A1), it is clear that for small enough r, the interior of a circle in the z-plane is mapped onto the interior of a circle by the Möbius transformation. In addition, the point $\frac{b}{d}$ is inside it. At some point, for sufficiently large r, the Möbius transformation transforms a circle to a half-plane, that is, a circle with an infinite radius. In case r is further increased beyond this value, the interior of the circle in the z-domain is mapped onto the exterior of the circle in the P-domain. Note that in this case, the point $\frac{b}{d}$ is in the exterior of this circle in the P-domain, as well as all the images of smaller circles in the z-domain.